Materials Today Nano 29 (2025) 100553

Contents lists available at ScienceDirect

Materials Today Nano

journal homepage: www.sciencedirect.com/journal/materials-today-nano

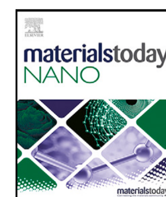

Nano-patterning using ultra-thin alumina membranes

Claudia Fernández-González [a,*], Sandra Ruiz-Gómez [a,b], Ana Arché-Núñez [a], Lucas Pérez [c,d,*], Célia Tavares de Sousa [e]

[a] ALBA Synchrotron Light Facility, CELLS, Cerdanyola del Vallès, 08290, Spain
[b] Max Planck Institute for Chemical Physics of Solids, Dresden, 01187, Germany
[c] Dept. Física de Materiales, Universidad Complutense de Madrid, 28040 Madrid, Spain
[d] Instituto Madrileño de Estudios Avanzados - IMDEA Nanociencia, 28049, Madrid, Spain
[e] Dept. de Física Aplicada, Facultad de Ciencias, Universidad Autónoma de Madrid (UAM), Campus de Cantoblanco, 28049, Madrid, Spain

ARTICLE INFO

Keywords:
Nanopatterning
Ultra-thin alumina membranes
In-situ anodization
Transference ultra-thin alumina membranes
Ordered arrays of nanostructures

ABSTRACT

With the mass production of well-controlled and low-cost nanostructures on the horizon, considerable attention has been given to porous anodic alumina (PAA) templates to assist in the fabrication of both individual and ordered nanostructured objects – particles, rods, wires, and holes – with applications in electronics, data storage, bioengineering, and nanomedicine. The fabrication of free-standing PAA templates, several microns thick, as well as their applications, have been largely described in the literature. In recent years, research has focused on the synthesis of ultra-thin anodic alumina membranes (UTAMs), making them compatible with top-down fabrication and large-scale production. The ability to obtain these nanostructures on different surfaces, including glass, silicon wafers, or flexible substrates, extends their range of applications, enabling the integration of nanostructured materials on top of thin layers and allowing for the precise tuning of the physical and chemical properties of the materials. This review focuses on this new and promising nanopatterning approach to fabricate large areas of ordered nanostructures using UTAMs as patterning masks. We report the most recent advances in the synthesis of UTAMs, focusing on two different approaches: *in-situ* anodization of thin aluminum films on various substrates and deterministic transfer of UTAMs onto a desired substrate. In the first case, we collect information regarding substrates, buffer layers, growth of Al films, anodization, and the post-treatment of the UTAMs. In the second case, we focus the review on the synthesis of UTAMs and, especially, on the transfer process to the substrate. For both methods, we compare the results regarding the nanostructure's self-organization and the control of size, shape, and spacing. Finally, we will review several applications in which the use of UTAMs plays a key role in the performance of nanostructured devices.

1. Introduction

1.1. Nano-patterning

Precise control of dimensions and the physical–chemical properties of materials at the nanometer scale remains a central issue in nano-devices, including nano-electronics, nano-optoelectronics, and sensing. This requires the development of surface nano-patterning techniques to obtain large-scale arrays of low-cost nanostructures [1]. Considering that, in most cases, the properties of patterned nanostructures are critically dependent on the size, shape, and regularity of their substructure on the micro- and nanometer scale, it is essential to develop one- [2,3], two- [4–7], or three-[8–10] dimensional architectures with precise uniformity and well-defined, controllable characteristics. These structures should be fabricated using versatile patterning techniques compatible with a wide range of materials. The regularity of the patterns also facilitates experimental studies of these systems, as well as theoretical approaches and simulations. Moreover, for technological applications, nano-patterning techniques need to be low-cost and allow for high fabrication throughput of large pattern areas [11].

Periodic micro and nanostructures can be produced using a top-down approach, starting from bulk materials or continuous sheet films, followed by milling or lithography to create the desired pattern. These top-down techniques provide precise control over the size, shape, and spacing of the nanostructures, making them ideal for applications that require the fabrication and manipulation of single nanostructures. They also allow for high uniformity during the fabrication process. However, conventional lithographic techniques are rapidly approaching their practical limits for fabrication in the sub−100 nm range, presenting a key challenge in the current top-down nanotechnology [12].

* Corresponding author.
E-mail addresses: cfernandez@cells.es (C. Fernández-González), lucas.perez@ucm.es (L. Pérez).

https://doi.org/10.1016/j.mtnano.2024.100553
Received 3 September 2024; Received in revised form 4 December 2024; Accepted 15 December 2024
Available online 23 December 2024
2588-8420/© 2024 The Authors. Published by Elsevier Ltd. This is an open access article under the CC BY-NC license (http://creativecommons.org/licenses/by-nc/4.0/).

Recent advances in nanolithographic techniques [13], such as ion- and electron-beam lithography [14–16], X-ray lithography [17], and scanning probe techniques [18,19] have enabled access to structures on the sub−100 nm size scale. However, these methods remain limited in terms of the area that can be nanostructured, and are still expensive and time-consuming, and require state-of-the-art facilities for large-scale patterning. Moreover, top-down processes are often tedious and labor intensive, which limits their widespread adoption for large-area applications [12,20]. To reduce time and costs while increasing nanostructured areas, some researchers propose the combination of both, the top-down techniques with the bottom-up approaches, described below. In this way, top-down techniques would expand accessible geometries, whereas bottom-up techniques would reduce processing time [21,22].

The bottom-up approach begins with individual building units that are structures at the sub-nm and nanometer scale, such as atoms, molecules, polymers, and colloids. By controlling the assembly of these building units, the desired nanostructured materials can be obtained. Controlling particle size, shape, and crystalline structure represents some of the key challenges in bottom-up techniques. Over the last few decades, a wide variety of approaches have been developed to control the size, shape, and periodicity of nano-patterning, including block copolymer [1], sol–gel [23], molecular self-assembly [24,25], DNA scaffolding [26,27], and anodic porous templates [28].

Typically, the main disadvantage of these techniques is related to the broad size distribution and limited control of the obtained nanostructures. However, extensive research in this field has demonstrated that nanomaterials obtained using the bottom-up approach hold promising applications across a range of diverse fields due to their ability to form organized one-, two-, and three-dimensional periodic nanostructures.

1.2. Porous anodic alumina membranes

A successful example is the porous anodic alumina (PAA) templates, which have become widely used due to their easy fabrication, high pore density arranged in ordered close-packed hexagonal arrays, and the further possibility to tailor pore diameter and length [29,30].

The pore diameter of the PAA resulting from the electrochemical anodization depends on the anodization voltage and covers a range from sub−10 nm to 700 nm [31–34]. Adjusting the anodization conditions, these templates can present a highly ordered hexagonal array of pores. The pores are highly monodispersed, and pore density ranges from 10^9 to 10^{12} pores/cm^2, whereas a porosity of 10% is observed in a perfect hexagonal arrangement of nanopores formed by self-organized membranes [35]. However, since the pore diameter can be varied by the widening process, which is based on the chemical etching of porous alumina walls in acidic solutions, the membrane porosity can be increased up to 70% [36–38]. The length of the pores can be varied from a few nanometers to a hundred micrometers.

PAA membranes have been extensively used for synthesizing high-aspect ratio nanostructures, particularly in combination with template-assisted electrochemical deposition [39–41]. The possibility of growing larger arrays of ordered nanowires has been essential, for example, in the field of magnetism, in which long-range interactions play a key role in the collective behavior of nanostructured systems. In magnetic systems, precise control over the geometry and distribution of nanostructures is essential for tailoring the physical properties of the nanosystems [42,43]. As a result, PAA membranes have been used, in combination with physical deposition techniques, to produce nanostructured thin films [44,45] and ordered arrays of antidots [46–48] controlling the magnetic and magnetotransport properties of the different systems through the geometry of the PAA membrane used as substrate.

PAA templates have also been used in tissue engineering [49], filtration [50] and the synthesis of nanostructured thermoelectric materials [51,52] and nanostructured biomedical electrodes, [53,54] among other applications [55,56]. In combination with atomic layer deposition, PAA membranes can be used to produce nanotubes [57], expanding the potential applications of these nanostructures.

Going one step further, the shape of the nanopores can be controlled designing unequal aluminum anodization rates at different anodization voltages, starting from designable templates [58]. In addition, PAA also enables the assembly of interconnected and hierarchically branched nanopores, as well as three-dimensional arrays of pores with controlled connectivity [55,59,60]. The possibility of producing three-dimensional alumina templates introduces a new degree of freedom in controlling the magnetic properties of nanostructures [61,62] or enables the development of 3D metamaterials, whose color can be tailored by adjusting the geometrical parameters of the PAA template [63].

1.3. Nano-patterning with Ultra-Thin Alumina Membranes

Ultra-Thin Alumina Membranes (UTAMs) are a specific type of PAA membranes characterized by a small thickness ranging from several hundred nanometers to few microns. The total area of these membranes can be as large as several square centimeters. The small thickness of UTAMs makes them compatible with top-down techniques, where they can be used as masks to grow nanostructures by physical techniques (i.e., e-beam evaporation or sputtering). The recent advances in the synthesis of UTAMs also make them compatible with large-scale production of low-cost nano-patterned surfaces with tunable dimensions and physical properties that have already been employed to synthesize a wide variety of ordered nanostructures.

Compared to other nano-patterning methods such as e-beam lithography and self-assembly processes, the UTAM nano-patterning approach presents several advantages: (i) as in the PAA templates, the pore diameter can be easily adjusted from sub-10 to 700 nm by changing the anodization conditions; (ii) the pore length can also be adjusted from several hundred nanometers to few microns; (iii) a broad range of materials (e.g. magnetic, semiconductors, polymers, metals) with different shapes (e.g. wires, tubes, rods, discs) can be grown inside the UTAM pores; (iv) large areas of several square centimeters can be patterned with high throughput and low equipment costs; (v) ultra-high density of the ordered nanostructures (10^9-10^{12} pores/cm^2) compatible with the requirements for high-density data storage media, photonic crystals, and high-sensitivity sensors; (vi) compatibility with a broad range of substrates.

The recent advances in the synthesis of UTAMs also make them compatible with the mass production of well-controlled and low-cost nanostructures on the horizon for several applications in electronics, data storage, bioengineering, and nanomedicine.

This review will focus on the most recent achievements in nano-patterning to fabricate large areas of ordered nanostructures using UTAMs as fabrication masks. We report the main synthesis methods of UTAMs, focused on two different approaches: *in-situ* anodization of aluminum thin films on different substrates and anodization of Al foils followed by the transfer onto a desired substrate. Regarding the first method, we will report the substrates selected related to the final application, the techniques used to deposit the aluminum films, and the different anodic parameters, as well as the UTAMs post-treatment. The review of the second method will focus on the synthesis of UTAMs and especially on the transfer-to-substrate process. For both methods, we will compare the results regarding the nanostructure self-organization and the control of size, shape, and spacing. We will also discuss the best strategies to obtain large-scale UTAMs in the range of square centimeters on any substrate in a mass-production way. Finally, we will review the main applications of these self-assembled templates in different technological fields, namely the synthesis of magnetic dots for magnetic recording, plasmonic nanorods for sensing, and arrays of nanoelements for energy storage and conversion, as well as biomedical applications.

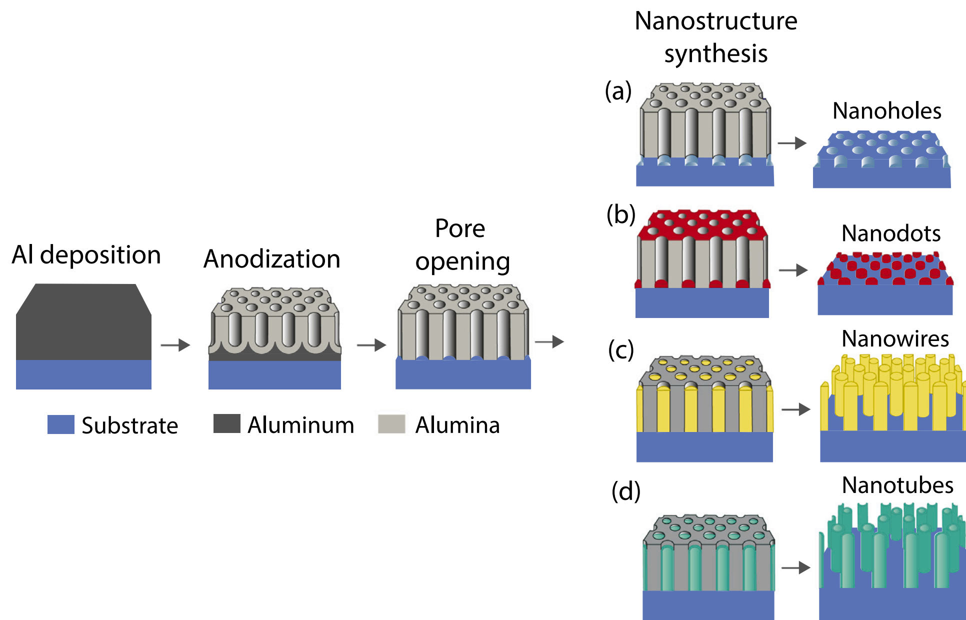

Fig. 1. Schematics of the different nanostructures that can be fabricated using UTAMs: (a) nanoholes in a substrate by etching through the pores of the UTAM; (b) nanodots or antidots by evaporating material from the top of the template using Physical Vapor Deposition techniques; (c) electrodeposited nanowires grown through the pores of the UTAM; (d) nanotubes synthesized by Atomic Layer Deposition.

2. *In-situ* anodization of ultra-thin aluminum films

PAA membranes are typically prepared on Al foils, which are subsequently removed to yield freestanding nanoporous templates. However, the ability to anodize an aluminum layer deposited directly onto a substrate significantly expands the potential applications of these templates, paving the way for novel nanostructuring technologies and related applications. *In-situ* anodization of Al layers on metallic surfaces allows for the creation of nanoporous alumina templates that are strongly bonded to the substrate, enhancing the likelihood of achieving well-ordered nanostructures on the surface. As illustrated in Fig. 1, once a UTAM is prepared on a specific substrate, different strategies can be employed to produce different nanostructures on the substrate surface. For example, etching the pores can create patterned substrates, while filling the pores using vacuum-based growth techniques or electrodeposition can result in the formation of nanoparticles (NPs) [64], nanodots (NDs) [65,66], nanowires (NWs) [67,68], nanotubes (NTs) [69–71] and other nanostructures [72,73].

Moreover, since it is feasible to anodize large Al surfaces, large ordered arrays of nanostructures can be fabricated, thereby integrating PAA-related nanofabrication techniques with existing very large-scale integration (VLSI) technologies [74,75]. This section reviews the main approaches used to synthesize UTAMs on top of different materials.

2.1. Substrates

The quality of the UTAM is closely linked to the morphology, structural, and surface properties of the initial Al layer, which, in turn, depends on the substrate material onto which the Al is deposited. It is essential to have an Al layer that is as flat as possible covering the outermost layer of the substrate to ensure the homogeneity of the anodization process. The surface homogeneity and roughness of the starting Al will depend on the surface properties of the substrate. Therefore, careful selection of the appropriate substrate is crucial. This choice is influenced by the intended application of the UTAM (e.g., electronic devices, optoelectronics, energy, biomedical applications) and encompasses a variety of materials, ranging from rigid conductive and semiconductive substrates to transparent conductive oxide glasses and flexible polymers [76–78].

The fabrication of UTAMs on semiconductor substrates has been well-established for applications in electronic devices. Most electronic components are based on Si, the most widely used material in integrated circuit fabrication. Consequently, the ability to synthesize nanostructures on Si surfaces is crucial for integrating nanoelements into electronic devices. As a result, Si is one of the most commonly used substrates for *in-situ* anodization. Several types of crystalline Si (intrinsic, n-type, p-type) can be utilized, with p-doped Si being the most extensively studied [79]. It is important to note that due to the differing electrical resistivity of Al and Si, the anodization process in this supporting material only proceeds until the Al–Si interface is reached. While the electrolytes typically do not etch n-type Si, they do react with p-type Si [80], which may necessitate substrate protection. To shield the Si substrate from the chemical etching effects of acidic electrolytes, a Si oxide layer can be created for passivation [81–83]. SiO_2 protective coatings can be obtained through the thermal oxidation of Si substrates. Additionally, Si surfaces can be protected by introducing H atoms that are covalently bonded to surface Si atoms (H-terminated Si), which enhances surface stability [84].

GaAs is another semiconductor widely used in the microelectronics industry and has also been employed as a substrate for UTAM fabrication. Similar to p-type silicon, GaAs is etched by the electrolytes during the anodization process, allowing for selective etching of the substrate surface. This enables the creation of an ordered array of nanoholes in the semiconductor surface [77,85].

Nanostructures are also extensively utilized in photonics, where transparent substrates are essential. Glasses (quartz- and borosilicate-based) are commonly used in this field due to their favorable optical properties (i.e. high transmittance, low self-fluorescence, and low optical absorption) and thermal stability. Given that electrical conductivity is also required for the anodization process, metal-coated glass substrates [68,86,87] are often used. Transparent conductive oxides (TCOs) are also suitable substrates for the preparation of UTAMs [88]. These oxides, such as In_2O_3, SnO_2, and ZnO, are doped with donor impurities (e.g. F, In, Ga, Ti) to increase the density of free carriers, achieving low electrical resistivity values (10^{-3} to 10^{-4} Ω cm). Two of the most commonly used TCOs in optoelectronics are indium tin oxide (ITO, In_2O_3:Sn) and F-doped SnO_2 (SnO_2:F) [89,90].

These materials, with large enough electrical conductivity and optical transparency, can be easily grown as thin films, and it is possible

to fully anodize the Al layers to produce UTAMs on top of them. M. Houng et al. [87] accomplished a comparative study of the anodization of the ultra-thin Al layer deposited over uncoated and ITO-coated glass, observing that ITO becomes conductive and ensures the electric contact with the Al until the end of the anodization process. In insulating substrates such as uncoated glass, part of the Al between the pores is not in direct contact with the electrolyte and, therefore, remains as a final product in the UTAM.

In addition, the chemical stability of glasses makes them suitable substrates for the synthesis of UTAMs where biocompatibility is required, i.e., biological applications [91]. However, in many applications, the substrate should be flexible to conform to the shape of the tissue where it is incorporated. In these cases, polymeric substrates are used. One of the most versatile polymers is Polydimethylsiloxane (PDMS) [78] due to its flexibility, chemical stability, and low toxicity. Other metallic materials (titanium and titanium alloys [92]) are well-known in the field of biomedicine. They improve the surface adherence between the metallic surgical implants and the cellular tissue and are also used as support substrates for UTAMs [92].

2.2. Buffer layers and interlayers

There are several reasons to add, in most cases, buffer layers (also called interlayers) between the substrate and the Al thin layer to improve the UTAM preparation. The main reason to include them is to improve the adhesion between the substrate and the Al layer. The atoms of the selected material should increase the binding energy between the substrate and the upper layer to enable the growth of thicker Al films, since the adhesion drops by increasing the thickness due to the film strain [93,94]. This adhesion layer also avoids the burst and the peel-off of the alumina layer during the anodization process [95,96]. The interlayer offers the opportunity to tune the properties of the UTAM, which is required in some applications. As will be described in detail in Section 2.4, once the Al layer is fully oxidized, the electrolyte can reach the material acting as a buffer layer and start oxidizing it. Depending on the interlayer material, different oxides are synthesized with different morphologies [97,98]. In addition, the shape of the barrier layer can be modified and even removed by varying the anodization parameters, enabling the channels in the UTAM to directly reach the substrate [99–101]. In the case of using semiconductors and insulators as substrates, the interlayer acts as a conducting electrode for the anodization process as well as a working electrode for a subsequent electrodeposition process to fill in the pores [102,103]. Once the anodization process is finished and the alumina barrier layer is removed, the metallic layer allows good electric contact, making it possible to fill in the pores with metallic materials using electrodeposition. This conducting interlayer also opens the possibility to connect the nanostructures with the substrate. This could be crucially important in applications where the nanostructures and the substrate are part of an electrical device, and a good electric contact is needed [86,104–106].

As will be described later, one of the critical steps in the fabrication of UTAMs is the deposition of high-quality Al films. In some cases, it is necessary to thermalize the substrate to get uniform layers. In particular, the aluminum crystallization is strongly affected by the difference in thermal conductivity between the deposited metal, normally Au (318 W/mK), and the substrates, commonly SiO_2 (1 W/mK) or glass (0.8 W/mK). The introduction of a metallic interlayer with an intermediate thermal coefficient like Ti (21.9 W/mK) or Pt (71.6 W/mK) prior to the Al deposition improves thermal dissipation and consequently, the Al crystallization [107,108].

Finally, the interlayer can be used as a tool to sense when the Al layer is fully oxidized, allowing it to stop the anodizing process just when it reaches the interlayer. This also enables an accurate calibration of the anodization rate. The latter is only possible if the difference between the oxidation potentials of the involved materials is considerably different [109–111]: when the Al layer is completely anodized, the electrolyte becomes in contact with the interlayer and the current density abruptly changes. This drop in the values of the current density can act as a trigger to stop the anodization process [112].

Metallic materials used as interlayers can be divided into two groups: valve and non-valve metals. Valve metals are so called because they do not allow current to pass along one direction [113]. Materials from groups IV and V of the periodic table of elements (Ta, Nb, Zr, Al, Ti, Hf, and W) are valve metals. As mentioned above, one of the most important characteristics of the valve metals is the electrochemical rectification properties of the oxide layers formed on the metal surface, which means that for the same current values applied with opposite polarity, the anodic voltage is considerably higher than the cathodic voltage [114]. When a valve metal is in contact with an aqueous solution, the reaction with oxygen or water leads to the formation of a surface oxide layer. This oxidized dense passive layer shows exceptional resistance towards corrosion in many aggressive environments and works as a protective layer. During the anodization process, this oxide acts as a barrier layer through which the oxygen ions electromigrate from the electrolyte to the metal surface, reducing the rate of further oxidation to very low values [115].

Non-valve metals (i.e. Cu, Ag, Au, Pt) some of them are noble metals belonging to groups X and XI. Contrary to valve metals, they do not tend to form oxides; they are relatively inert and corrosion-resistant. These metals have low electrical resistivity (on the order of 10^{-10} Ω cm) and, therefore, are often used as electrical contacts, current collectors, and as the nucleation layer for the growth of one-dimensional nanostructures [116]. It is important to note that when the supporting material is a doped semiconductor, and if the final application is the integration of nanostructures in electronic or optoelectronic devices, special attention should be paid to the interlayer material. Different metal/semiconductor heterojunctions can be obtained, affecting the performance of the final device [86,106].

As shown in Table 1, most of the buffer layers are grown using Physical Vapor Deposition techniques (RF, DC magnetron, reactive, and ion sputtering) under vacuum conditions, in the same system where Al is evaporated afterward to avoid interlayer oxidation. Nevertheless, wet techniques like spin-coating have been used in particular cases, for example, TiO_2 (titanium oxide) coatings on ITO substrates [117].

Besides the important role that valve metals have been used as adhesive layer, they can also be used as intermetallic inhibitors to avoid diffusion between non-valve metals (used as metallic contacts) and aluminum films. If diffusion between non-valve metals and aluminum occurs, oxygen reactions can take place, leading to the breakdown of the UTAM template. In addition to limiting the formation of intermetallic compounds and providing good mechanical adhesion characteristics, the valve metal should ensure that: (1) the anodized barrier layer suppresses the Oxygen Evolution Reaction (OER) to allow field-driven barrier layer removal of alumina at pore bases, and (2) the formed oxide layer is stable and suitable for selective etching by an *in-situ* technique [99].

Titanium is one of the most common valve metals used as interlayer material [81,95,100,103,104,116]. In addition to its excellent adhesion to Al and most substrates, intermetallic phases containing Ti and non-valve metals are normally formed at temperatures above 500 °C, and Al–Ti compounds at temperatures above 350 °C. These high-temperature values ensure that no intermetallic compounds are formed during the synthesis process. Moreover, TiO_2 has a small bandgap compared to other valve metal oxides (Ta_2O_5, WO_3, Nb_2O_5) [148,149] which results in a lower breakdown voltage, enabling easier oxide removal at the bottom of the pores of the PAA template using electrochemical etching [150].

Tantalum is also used as a single interlayer [120]. It is a refractory metal that presents good adhesion, high toughness, ductility, and provides uniform coatings. Due to its low electrical resistivity and corrosion resistance [151,152], it is used in *in-situ* anodization as a

Table 1
Summary of the substrates, buffers and interlayers used in *in-situ* anodization of UTAMs.

Substrate	Buffers and Interlayers	Deposition method	Final Application	Ref.
Si	Au (100 nm)/Ti (10 nm) Pt (100 nm)/Ti (10 nm)	e-beam	–	[116]
Si + SiO_2	Nb (200 nm)	RF sputtering	–	[83,118]
Si	Nb (30 nm)/Au (50 nm) /Ti (6 nm)	–	Electrode for spin torque oscillators	[104]
Si	Nb/Au/Ti	–	Electrodeposition of NWs	[105,119]
Si	Ti (5-10 nm)/Au (10-50 nm)	DC magnetron sputtering	Electrodeposition of NWs	[102]
Si (100 nm) + SiO_2 (120 nm)	Ti (80 nm)	e-beam	Electrodeposition of NWs	[100]
Si + SiO_2	Ti (250 nm)	e-beam	Electrodeposition of NWs	[103]
Si	Ta (200 nm)	–	Electrodeposition of NWs	[120]
Si + SiO_2	Nb (100 nm)	RF sputtering	Study of barrier layers	[101]
Si + SiO_2	Ti (400-500 nm)	e-beam	Carbon NTs for biosensing	[121]
Si + SiO_2 (50 nm)	Ti (150 nm)	e-beam	Carbon NTs	[122]
Si	W (1000 nm)	DC sputtering	Electrodeposition of NWs	[123]
Si	Nb (400 nm)	Sputtering	Electrodeposition of NWs	[107]
Si	Au	–	Electrodeposition of NWs	[124]
Si	Ti (20 nm)	e-beam	–	[125]
p-Si (100)	TiN (100 nm)	PVD	–	[126]
p-Si	Ti (20 nm)	e-beam	–	[95]
p-Si (100) + SiO_2 (1.5 μm)	Ti (10 nm)/Au (200 nm)/Ti (10 nm)	Sputtering	Microelectrodes for neural sensing	[81]
p-Si	Ti (300 nm)	RF sputtering	Ni NWs magnetic storage devices	[67]
p-Si (100)	Ti (20 nm)	RF sputtering	Electrodeposition of nanostructures	[127]
p-Si (100)	Ti (20 nm)	RF sputtering	ZnO nanorods-electrodeposition	[128]
p-Si (100)	TiN (30 nm)	Reactive sputtering	Nanodot TiO_2	[66]
p-Si (100) + SiO_2	TiN (250-300 nm)	RF magnetron sputtering	–	[129]
p-Si (111)	Au	Thermal evaporation	–	[130]
p-Si (100)	Au (20 nm)	e-beam	Electrodeposition of CdS NWs	[110]
p-Si	Nb (100 nm)/Au (100 nm)	RF sputtering	–	[131]
p-Si	Ti (300 nm)	RF sputtering	Electrodeposition of NWs	[132]
p-Si + SiO_2	Ti (300 nm)	RF sputtering	Electrodeposition of NWs	[133]
n-Si and p-Si	Ti (5 nm)/Au (20-50 nm)	Evaporation	Electrodeposition of NPs	[64]
n-Si	Ti (100 nm)	DC sputtering	–	[134]
n-Si + SiO_2 (500 nm)	Ti (10 nm)	Thermal evaporation	–	[82]
n-Si	Pt (40 nm)/Ti (8 nm)	e-beam	–	[99]
n-Si (100) + SiO_2	Ti (200 nm)	Thermal evaporation	Study on the preparation of PAA	[135]
n-Si	Pt (50 nm)/Ti (40 nm)	e-beam	Electrodeposition of NWs	[136]
n-Si	–	DC magnetron sputtering	WO_3 coatings	[137]
Si + SiO_2 (100 nm)	Ti, W or Hf (150-200 nm)	DC magnetron or ion beam sputtering	Au pillars on top of nanorod oxides	[138]
n-Si + SiO_2 (500 nm)	Ti (20 nm)/W (60-200 nm)	Sputtering	WO_3 nanorods, nanocapsules and nanotubes	[139]
H-terminated n-Si	Ta (50 nm)/Au (50 nm)	Sputtering	NWs for magnetic recording	[84]
Glass + ITO and Si	TiO_2 (50 nm)/Ti (0.2-0.5 nm, 2-10 nm)	e-beam	Electrodeposition of nanorods	[96]
Glass and Si	Ti (2-5 nm)/Au (5-20 nm)/Ti (2-5 nm)	e-beam	Electrodeposition of nanorods	[140]
Glass + SiO_2 (23 nm) + + ITO	–	Magnetron sputtering	–	[141,142]
Glass + ITO (450 nm)	Ti (0.3, 1 and 10 nm)	Ion sputtering	–	[143]
Glass + ITO (450 nm)	Cr (0.3, 1 and 10 nm)/Ti (0.3-10 nm)	Ion sputtering	–	[143]
Glass + ITO (150 nm)	Ti (0.5-50 nm)	Sputtering	–	[109]
Glass + ITO	Ti (10 nm)	e-beam	Field emission electrodes	[118]
Glass	Nb (1-2 nm)	Sputtering	PAA for sensing applications	[144]
Glass	Ta_2O_5 (10 nm)/Au (5 nm)	Magnetron sputtering	Electrodeposition of nanorods	[145]

(*continued on next page*)

Table 1 (*continued*).

Glass + SiO_2 (15 nm) + + ITO (100-130 nm)	–	–	Synthesis of PAA	[97]
Glass	ITO (120 nm)	–	Synthesis PAA for optics	[87]
Glass + ITO	TiO_2 (30 nm)	e-beam	Growth of CdSe nanorods	[146]
Glass + ITO	TiO_2 (40 nm)	Spin coating	Photovoltaic devices	[117]
Fluorine-free Glass + I + ITO (130 nm)	–	–	Electrodeposition of NWs	[68]
PDMS	Au (50 nm)/Ti (5 nm)	DC magnetron sputtering	Growth on flexible substrates	[78]
TCO	NTO (Nb-TiO_2)	RF sputtering	TiO_2 growth of TiO_2 NTs	[88]
Sapphire	AlN (100 nm)	Reactive sputtering	Buffer layers for LEDs	[147]

conductive path for the electrochemical deposition of nanostructures within the pores of the UTAMs. It also acts as an effective diffusion barrier due to its high thermal stability in contact with Si and Al, ensuring that intermetallic compounds are not formed either with the substrate or with the Al thin film.

Tungsten is another intermediate material that can be deposited between the substrate and the Al layer [123]. One of the main advantages of W, apart from acting as an electrode for electrochemical synthesis, is that the WO_3 formed at the end of the anodization can be easily removed with neutral solutions (pH = 7). This opens the possibility of removing the oxide barrier layer at the bottom of the pores without etching the pore walls. Then, in another etching step, the pore size can be increased with high accuracy by etching with acidic solutions.

Nitrides have also been used as interlayers in the *in-situ* anodization of Al thin films [66,126,147]. In this case, it should be highlighted that the nitrides are one of the main components of the final device: their functionality goes beyond acting as an adhesive layer and/or contact path for UTAMs anodization. The aim of introducing these materials is to create a hexagonal pattern of holes or nanostructures on their surface, taking advantage of the natural periodicity of the UTAMs. The oxide template is removed after the anodization process, leaving the interlayer surface nanostructured. In this way, ordered hexagonal patterns can be created over large areas of the device using a low-cost route compared to conventional lithography techniques.

In addition to the chosen material, the thickness and surface roughness of the interlayers are also key parameters to consider. In particular, layers need to be thick enough to ensure adherence between the substrate and the UTAMs, but at the same time, thin enough to avoid peel-off caused by the surface stress generated during the deposition process. We can illustrate this effect by considering the thickness when using Ti as an interlayer [116] in the anodization of an Au/Ti/Al structure, for a wide range of Ti thicknesses. For thickness below 5 nm, all Ti was oxidized to TiO_2 during the anodization process. The Ti layer loses its adhesive benefits, and the UTAM template detaches from the underlying noble metal layer. For thicknesses between 5 and 20 nm, Ti is partially converted to TiO_2. The Ti directly beneath the PAA pores is anodized, but the Ti near the Au/Pt layer remains unaltered, bridging the porous structure to the Au/Pt interlayer. Finally, for thicknesses larger than 20 nm, thick TiO_2 barriers are formed. However, these layers cannot propagate further through the Ti. Table 1 summarizes the typical thicknesses found in the literature for the different interlayers. The values range from a few nanometers to a couple of microns for all of them, including valve, non-valve, alloys, and oxide materials. Different combinations of interlayers can also be used, as shown in Table 1. The number of interlayers varies according to the final application, ranging from one [124,125], two [96], three [81,140], and even no interlayers [68,97]. Valve metals are mostly used as single interlayers to improve the adhesion of the aluminum thin films to the different substrates [127,133]. When a good electrical contact is required for the synthesis of the nanostructures, a double layer is used, combining non-valve metal and valve metal to improve both conductivity and adherence. The most common pairs of evaporated metals are Ti/Au [64,78,99,102,116], Pt/Ti [99,116,136], and Ta/Au [84,145].

Trilayers are also commonly used to guarantee good electrical conductivity to carry out electrodeposition afterward to fill in the pores and obtain metallic nanostructures over the substrate surface. As mentioned before, Au is an excellent conductor, making it the most suitable material for acting as a working electrode in the electrodeposition process. However, the adhesion between Au and Al is not good enough. Therefore, interlayers (normally Ti) are used to ensure good adhesion between the substrate, the Au, and the Al layer [140]. These Ti interlayers are a few nanometers thick (between 2 and 5 nm) to keep the surface as flat as possible. Nb is also used as an interlayer in Nb/Au/Ti trilayers to improve the adhesion of the evaporated layers with the sample surface in cases where the synthesis process of nanostructures using connected UTAMs involves high temperatures (such as chemical decomposition and catalytic pyrolysis) [104,105,119]. Nb is selected because its thermal expansion coefficient is very close to that of aluminum oxide [153]. In this way, it is possible to avoid cracks and breaking of the template during the growth of nanostructures. Nb can also be incorporated as a dopant in the buffer layer to improve both physical adhesion and electrochemical stability of the template during the anodization process [88,101]. Nevertheless, it is important to take into account that, although trilayers are commonly used to guarantee good adhesion between the substrate/non-valve metal and non-valve metal/aluminum film interfaces, bilayer systems have several advantages compared with trilayers, namely, the possibility of having a thicker layer system, which keeps the surface flatter, and a shorter evaporation process, which facilitates the evaporation of all the materials without changing the pressure conditions of the PVD.

2.3. *The aluminum layer*

After selecting the most appropriate substrate, the next step in the process of synthesizing ultra-thin alumina membranes over a solid surface is the deposition of the aluminum (Al) film. The morphology of the Al film plays an important role during the anodization process. Therefore, choosing the appropriate technology and conditions for the growth of the Al film is crucial. In particular, to avoid problems during anodization and to obtain alumina templates without defects, highly smooth Al thin films free of hillocks and spikes should be prepared.

Among the different deposition methods employed to grow metallic films over substrates, physical vapor deposition (PVD) techniques are normally chosen for *in-situ* aluminum thin film anodization due to the high purity, cleanliness, and flatness of the grown Al, as well as the well-controlled thickness, which ranges from several angstroms to millimeters. Among PVD techniques, the most commonly used methods are thermal or electron-beam evaporation and sputtering. Sputtering, and in particular RF magnetron sputtering, is the most widely used technique when non-conductive substrates are employed because it allows the growth of both the interlayer and the aluminum film in the same chamber [154]. Sputtering also produces denser and thicker coatings. In contrast, thermal evaporation allows for lower deposition rates, leading to a smoother surface of aluminum thin films.

The substrate temperature during Al evaporation determines the grain size of the evaporated Al layer. This temperature influences the

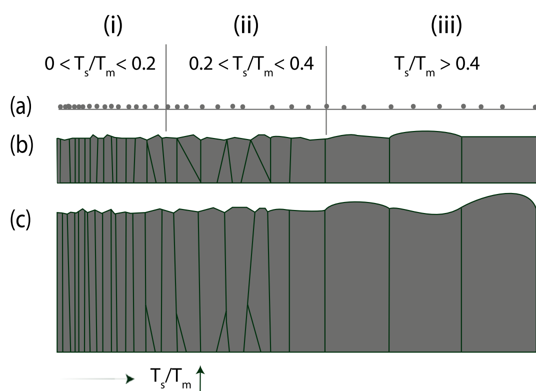

Fig. 2. Illustration of the Zone Model proposed by Movchan and Demichishin [155]. The schematics show the different morphologies that can be obtained by changing the ratio between the substrate temperature (T_s) and the melting temperature of the deposited metal (T_m) (i–iii), for different thin film thickness (a–c).

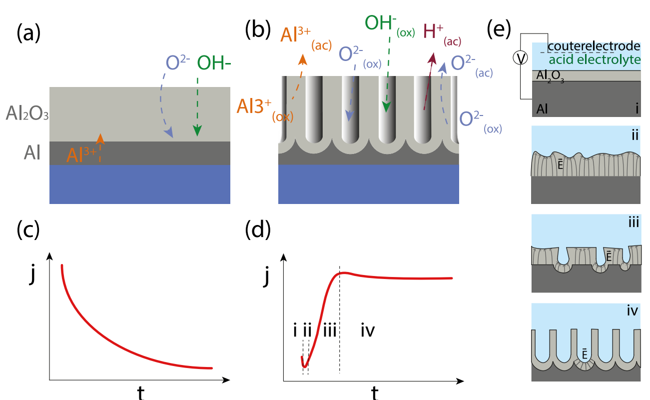

Fig. 3. Ion migration during the anodization of an Al layer in (a) basic or neutral electrolytes and (b) acid electrolytes. Evolution of current density during the anodization process for both (c) basic or neutral and (d) acid electrolytes. (e) Schemes of pore growth stages corresponding to the four different anodization regimes in acid media.

diffusion process of the adatoms on the sample surface, which can lead to different growth mechanisms. The Structure Zone Model proposed by Movchan and Demichishin [155] establishes a relationship between the substrate temperature (T_s) and the melting temperature of the metal to be deposited (T_m). Depending on the value of T_s/T_m, different diffusion processes occur during growth, resulting in different grain morphologies (see Fig. 2). For $0 < T_s/T_m < 0.2$ (region i), the microstructure is composed of individual and well-separated columns formed by differently oriented grains. Shadowing effects are characteristic of this zone because shadowed surface regions remain unfilled due to weak surface diffusion, which leads to higher surface roughness. The so-called zone T, corresponding to $0.2 < T_s/T_m < 0.4$ (region ii), is characterized by self-surface diffusion, in which adatoms move over the surface of the sample until they find the most stable position to condense, allowing for surface recrystallization. The morphology is represented by V-shaped columnar grains at the top of the substrate. Finally, for $T_s/T_m > 0.4$ (region iii), diffusion becomes significant, and the grain boundary participates in the movement of adatoms, enabling the growth of large grains at the expense of smaller or unfavorably oriented ones. It is important to note that the larger the grains, the higher the surface roughness [156]. Better surface flatness of evaporated thin films is achieved by synthesizing at temperatures in the range of Zone T. The contributions of the shadowing effect and grain growth are minimized in this temperature region, resulting in conditions that are best suited for fabricating connected UTAMs.

Lita and Sanchez conducted a study to determine the effects of temperature during the deposition of Al polycrystalline thin films [157]. They concluded that the T_s/T_m ratio should be greater than 0.2 to allow for self-diffusion and boundary motions, while remaining low enough (below 0.4) to avoid the formation of large grains, which would increase film roughness. It should be noted that, for Al evaporation, these values are achieved while keeping the substrate at room temperature. It should also be considered that the substrate may warm up during growth, particularly when using sputtering at high deposition rates. In these cases, a negative voltage bias can be applied to the substrate [158]. The Ar^+ bombardment caused by the bias effect produces re-sputtering and removes aluminum atoms from the hillock, leading to a flat aluminum thin film surface. In general, surface roughness increases with thickness and grain size: Al layers with small grains tend to be smoother than those with larger grains [83]. Therefore, the different parameters of growth techniques should be adjusted to achieve the lowest roughness for a particular Al thickness.

2.4. Anodization process

Anodization of aluminum in aqueous electrolytes gives rise to anodic oxide films with two different morphologies: the use of neutral or slightly acidic electrolytes (pH 5-7) allows for the formation of nonporous barrier-type oxide films [159,160] (Fig. 3a), whereas the use of acidic electrolytes (pH < 5) produces PAA templates [30,161,162] (Fig. 3b). The growth kinetics in both cases are different. In barrier-type oxide formation, the current density under potentiostatic conditions, as well as the growth rate, decreases exponentially with time (Fig. 3 c). The high pH of the electrolyte leads to limited field-assisted alumina dissolution, and the reduced alumina dissolution rate, compared with its formation rate at the metal/oxide interface, limits the maximum thickness, which is proportional to the applied voltage. In this case, anodic alumina grows simultaneously at the oxide/electrolyte interface and at the metal/oxide interface, through Al^{3+} egress and O^{2-}/OH^- ingress under a high electric field [163,164].

In the case of porous-type anodization, the current density is constant during the anodization under potentiostatic conditions due to the constant thickness of the barrier layer at the bottom of the pores after the first steps of their formation (Fig. 3d). In this case, four different regions can be distinguished (Fig. 3e). In the first one (i), the current density *j(t)* rapidly decreases due to the formation of a high-resistivity oxide barrier layer. This drop in *j(t)* reaches a minimum value (region ii), which corresponds to the pore formation in the surface irregularities of the aluminum layer. These surface imperfections induce local heating due to the high local electric field. The increase in temperature enhances the chemical-assisted dissolution of the alumina. In region (iii), the current density increases, corresponding to the competition between the nucleation of new pores and the increase in size of the existing ones. In the last region (iv), the current density decreases slightly until reaching a constant value, when the equilibrium between the growth and dissolution of the alumina is reached. This steady value indicates the constant growth rate of the nanopores. The thickness of the porous oxide film is linearly proportional to the total amount of charge, i.e., linearly proportional to the anodization time, whereas the thickness of the barrier layer at the pore bottom is constant and proportional to the anodization voltage. In this case, there is a balance between the alumina formation at the metal/oxide interface via the inward migration of O^{2-}/OH^- and the field-assisted dissolution of the oxide at the electrolyte interface with the consequent release of Al^{3+} cations [165,166].

The formation of the anodic alumina membranes normally takes place through the following chemical processes: (1) a water-splitting reaction occurs at the electrolyte/oxide interface; (2) Al^{3+} ions form at the metal/oxide interface when the Al gets oxidized; (3) the Al^{3+} ions react with O^{2-}/OH^- ions that have migrated across the barrier layer due to the generated electric field; (4) if the H^+ concentration is sufficiently high (pH < 1.77), a field-assisted oxide dissolution of the alumina occurs at the pits of the oxide/electrolyte; and finally, (5) there is also hydrogen formation at the cathode.

(1): 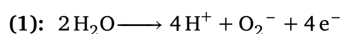
$$2\,H_2O \longrightarrow 4\,H^+ + O_2^{\,-} + 4\,e^-$$

(2): 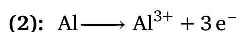
$$Al \longrightarrow Al^{3+} + 3\,e^-$$

(3):

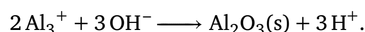
$$2\,Al_3^{\,+} + 3\,OH^- \longrightarrow Al_2O_3(s) + 3\,H^+.$$

(4): 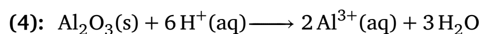
$$Al_2O_3(s) + 6\,H^+(aq) \longrightarrow 2\,Al^{3+}(aq) + 3\,H_2O$$

(5): 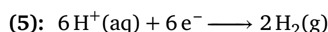
$$6\,H^+(aq) + 6\,e^- \longrightarrow 2\,H_2(g)$$

In the process, there is a balance between the growth of the PAA (3) and the oxide dissolution (4), with the individual rate of each step dependent on electrode kinetics, pH, temperature, and applied electric potential. This balance is needed for the formation of the porous structure since it makes the thickness of the barrier layer constant throughout the entire anodization process and hence allows steady-state pore growth into Al. The field-assisted dissolution of the oxide is the key parameter in the synthesis of porous alumina that separates it from the barrier-type alumina anodized in neutral solutions. Though the overall reactions depict a simple picture of the anodization process, the underlying chemistry and reactions involved are complex. The electrochemically active species, such as the oxygen anions or hydroxyl anions and the metal cations, must diffuse and migrate through the oxide for subsequent oxidation [165–167]. Since the oxidation reaction (3) occurs at the metal-oxide interface, whereas the dissolution of Al_2O_3 takes place at the oxide-solution interface, other anions, such as the acidic (or basic) counter ions and water molecules from the electrolyte, can also get incorporated into the forming oxide [168].

At the beginning of this process, the nucleation of the pores is randomly distributed on the Al surface. While the anodization proceeds, the pores grow and self-organize, increasing the regularity of the pore arrays. This regularity increases with the anodization time, resulting, in the case of a one-step anodization process, in a membrane with different ordering in the top and bottom parts. To obtain highly ordered membranes in hexagonal patterns, Masuda and Satoh proposed a two-step anodization process [169]. The two-step anodization process is schematized in Fig. 4. In the first anodization (i), the hexagonally ordered pores are formed only at the bottom layer by a self-organization process (a, d). Subsequently, the oxide layer is removed by wet chemical etching (ii). The remaining periodic pattern on the substrate acts as nucleation centers for the second anodization process (b, e). After the second anodization (iii), an ordered array of nanopores is obtained. The structure of the porous films formed after a two-step anodization is a closely packed regular array of hexagonal cylindrical pores normal to the Al surface (c, f). This porous structure extends from the surface of the oxide down to the oxide/metal interface, where it is sealed by a barrier oxide layer with approximately hemispherical geometry. The pore diameters and the pore densities of the alumina membrane can be precisely controlled by adequately varying electrochemical parameters, enabling the production of tailor-made templates, as explained in the following section.

2.5. Tuning the pore size, shape, and spacing

The structure of a PAA membrane can be defined by different parameters, such as interpore distance (D_{int}), pore diameter (D_p), barrier layer thickness (t_b), and pore wall thickness (t_w) (see Fig. 5a), pore density (ρ_p), and porosity (P). The values of these parameters depend on the anodization conditions, including the applied voltage or current, pH, type/concentration of the electrolyte, anodization time and temperature [30,170]. For an ideal PAA, the following relationship can be drawn by simple geometric considerations [35]:

$$D_{int} = D_p + 2t_w$$
$$\rho_p = \frac{2}{\sqrt{3}D_{int}^2}$$

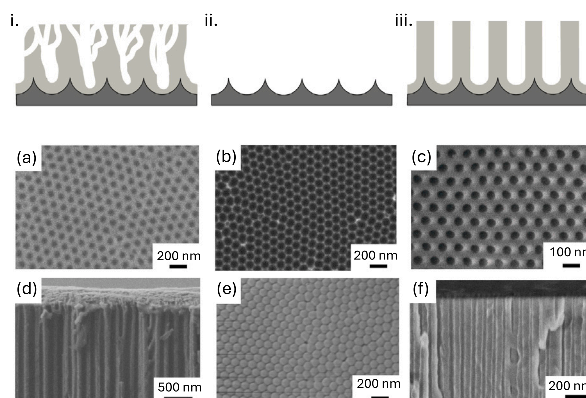

Fig. 4. Schematics of the cross-section of an Al foil sample during a two-step anodization process: i) first anodization, ii) alumina removal and iii) second anodization. Corresponding scanning electron micrographs of (a) top of alumina surface after first anodization, (b) patterned aluminum surface after alumina removal, (c) top alumina surface after second anodization, (d) cross-section of top alumina surface after first anodization, (e) bottom alumina surface after first anodization and (f) cross-section of the alumina membrane after second anodization.

$$P(\%) = \frac{\pi}{2\sqrt{3}}\frac{D_p}{D_{int}} \times 100$$

The pore diameter mainly depends on the anodization voltage and the electrolyte, making it possible to adjust it in the range of 6 to 900 nm (with pore widening) [165,171–173]. The pore diameter increases with the anodization potential [174] at a rate of 1.29 nm/V and with temperature, while it decreases with the pH of the electrolyte due to an increase in the dissolution speed of anodic oxide at the pore base [175].

Three types of electrolytes are commonly used for the preparation of the PAA templates, covering different ranges of pore diameters: sulfuric acid (D_p = 20 nm), oxalic acid (D_p = 35 nm), and phosphoric acid (D_p = 200 nm) [28,29]. In addition, pore diameter can be precisely tuned by the pore widening process. Moreover, it is also possible to generate complex arrays of pores with Y-branched, multi-branched, and tree-like multi-generation branched nanochannels, combining the widening process with a controlled reduction of the anodizing voltage [55,176]. It is well established that the interpore distance is linearly proportional to the anodization potential at a rate of 2.5 nm/V, although it can be slightly modified depending on the pH, temperature, and electrolyte. This rate value is only valid for mild anodization, where values of interpore distance between 35 and 980 nm can be achieved [165,171,172]. Since the voltage is maintained constant, a weak increase in D_{int} has been observed with increasing pH. Increasing temperature is equivalent to a decrease in pH in most cases [174].

The thickness of barrier-type alumina is mainly determined by the applied voltage, although there is also a small dependence on the composition of the electrolytes and temperature. The maximum attainable thickness in alumina has been reported to be less than 1 μm, corresponding to voltage values lower than 500 V. Up to this value, the breakdown of the barrier was observed [168]. In the case of porous alumina, the current density in the steady-state regime and the total amount of oxidized aluminum increase with increasing applied voltage, as do both the oxidation and dissolution rates. Although the oxidation at the metal-oxide interface initially increases at a faster rate than the field-enhanced dissolution, equilibrium between both processes is achieved when the current density reaches the steady-state value, which corresponds to a constant value of the barrier layer thickness (t_b). For each voltage value in the self-ordering regime, equilibrium is reached when t_b achieves the maximum thickness, establishing a direct dependence of t_b on the voltage. The reported values for t_b for various electrolytes are approximately 1.05–1.2 nm/V, although these values

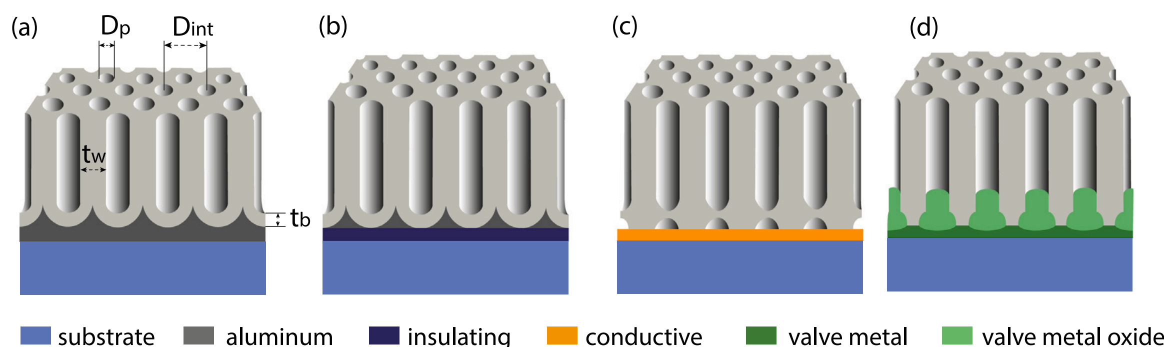

Fig. 5. Morphology of the interphase alumina-substrate for the different substrates and interfaces described in the text.

depend on the pH, temperature, and electrolyte [30,174]. At constant anodization potential, an increase in pH leads to a decrease in the alumina dissolution rate due to the reduced concentration of H^+ in the electrolyte. The decrease in the alumina dissolution rate, compared with its formation rate, results in an increase in t_b [161]. With an increase in temperature, the dissolution current density increases, and t_b has a weaker decrease.

It is important to note that in the particular case of connected UTAMs, once the aluminum layer is consumed in the anodization process, the electrolyte reaches the interlayer material and starts oxidizing it. This introduces a new variable because different oxides are obtained with different morphologies (depending on the interlayer material). By varying the anodization parameters and the underlying material, the barrier morphology can be modified and even broken at the interlayer. The barrier morphology that can be found when anodizing Al thin films in H_2SO_4, $H_2C_2O_4$ and H_3PO_4 electrolytes depends mainly on the substrates and interlayers in the following way:

- Insulating substrates (such as SiO_2, or glass) [136,177,178]: In this case, the U-shape of the barrier layer is very similar to the one formed in PAA from bulk Al foils (Fig. 5a). As shown in Fig. 5b, residual Al remains unoxidized between the alumina barrier and the substrate. These aluminum nanoparticles are mostly observed beneath pores with a smaller-than-average diameter. In this case, the anodization current drops to zero when the barrier layer reaches the insulating material, indicating the end of the anodization process.
- Substrates coated with conductive layers (e.g. Si, Pt, Au) [68,74,142,146,179,180]: Contrary to the previous case, the U-shape of the barrier layer is inverted, with voids between the barrier and the substrate (see Fig. 5c). Different explanations about the void formation can be found in the literature [181,182]. Seo et al. [181] attribute the formation of the cavities to a mechanical stress produced during the anodization. The conductive interlayer material allows for the complete oxidation of the aluminum layer, including the small Al particles that appear in the case of insulating substrates. These particles are firmly attached to the rigid substrate, and they cannot expand their volume when oxidized. It is necessary to restructure the interfacial void to create the additional space required. The formation of voids can also be detected in the anodization curve by a decrease in the current, which reduces the anodization rate. The anodization process proceeds as follows: first, the anodization takes place similarly to a conventional anodization of an Al foil. When the barrier layer reaches the interlayer material, it starts changing its shape to an inverted U due to the stress originated by the substrate stiffness needed to accommodate the volume expansion. At the same time, the anodization continues in the small Al areas that remain between the pores. The volume expansion of these small areas during their oxidation generates stress, pushing laterally the voids, which increases their curvature. On the other hand, Khatko et al.[182] consider the field-assisted dissociation of the Al–O bonds in the innermost part of the barrier layer the responsible mechanism of void formation at the interface alumina/conductive layer. When these Al–O bonds are broken, the electrons move by tunneling from 2p orbitals from the O^{2-} ions towards the positively charged Si surface within the void. In this way, a small fraction of the mobile O^{2-} ions are oxidized and oxygen atoms are formed and accumulate inside the voids.
- Substrates coated with valve metals (e.g. Ti, W, Ta, Hf) [96,143,183–187]: In this case, the formed pores are filled with oxide nanodots (Fig. 5d). When the pore formation is finished and the anodization continues, the O^{2-} ions reach the valve metal interlayer and start oxidizing it. This is reflected in the *j(t)* curves as an initial drop in the current density, followed by a gradual decrease towards a saturation value close to zero. This decrease in the current values also indicates that the valve metal oxide grows as a barrier-type layer filling the alumina pores. The growth of the valve metal oxide within the pores is self-limiting: the electric field across the oxide decreases as a result of thickening the oxide at a fixed anodic voltage. By choosing the appropriate anodization parameters and valve metal thickness, it is possible to fully oxidize the interlayer. For the case of W interlayers, this situation can be reached when anodizing in 55% H_3PO_4 while applying 86 V at room temperature for 19 nm thick films [184]. If the thickness is lower than this value, the resulting WO_3 is too thin, and the electric field across the oxide is large enough to drive O^{2-} ions to the substrate. If the substrate is conductive, the current density increases due to O_2 evolution from the substrate. To obtain thicker nanorods inside the alumina pores, a reanodization process at higher voltages can be carried out. One example is the work done by Mozalev et al. [188], where they reanodize a 300 nm thick tantalum layer under 310 V and, as a result, obtain an array of vertical tantalum oxide columns of 260 nm height over a continuous layer of tantalum oxide of approximately 260 nm thick, passing between the columns and the residual tantalum layer.

In addition to filling the pores with valve metal oxide nanostructures, the use of valve metals as interlayers allows for the modification of the morphology at the alumina/substrate interface. A. Mozalev and J. Hubalek provide a detailed explanation of the different morphologies that can be achieved depending on the metal and anodization conditions [138]. In particular, they studied the case of Si substrates covered with a single layer (W, Ti, Hf), a bilayer (W/Ti) or an alloy. During the anodization process, once the Al layer is completely oxidized, the acidic electrolyte reaches the valve metal, initiating its oxidation. If the anodization is stopped after the oxidation of several nanometers, valve metal oxide nanodots are formed (see Fig. 6(a,b). If the anodization of the valve metal continues, nanorods are formed inside the alumina pores. The morphology of these nanorods is characterized by concave areas at the alumina/valve metal

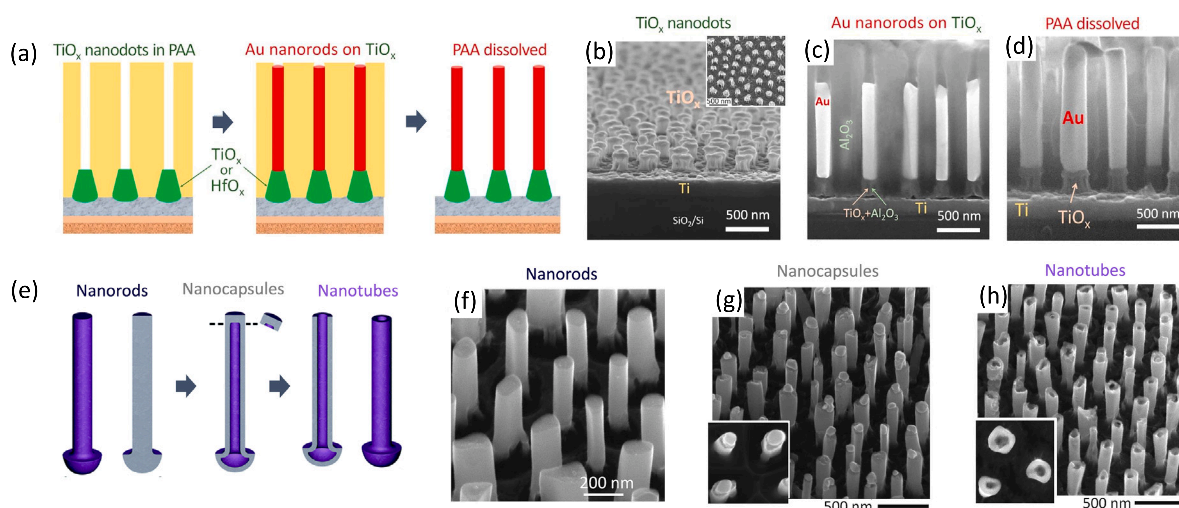

Fig. 6. (a) Schematics of valve metal nanorods used as working electrodes for the electrodeposition of metallic nanopillars. (b, c, d) SEM images of valve-metal oxide nanorods at the bottom of the pores, electrodeposition of Au nanopillars inside the alumina pores and free standing Au nanopillars after template removal, respectively. Reproduced from Ref. [138] with permission from Elsevier Ltd (2018). (e) Schematics of the modifications of the valve metal nanorods for their transformation in nanocapsules and nanotubes. (f, g, h) SEM images of the nanorods, nanocapsules and nanotubes, respectively. Reprinted from Ref. [139] with permission from The Royal Society of Chemistry (2016).

interface, which are deeper than those observed in the nanodot stage. The concave bottoms of the valve-metal nanorods can almost make contact with the conductive substrate, which is advantageous for further electrodeposition of metals. The use of valve metals can also widen the bottoms of the pores in UTAMs, improving the adhesion of the grown nanostructures to the substrate. Furthermore, the authors investigated the post-treatment of the valve metal oxides to use them as conductive electrodes for electrodeposition. They observed that the three valve metal oxides under study (WO_x, TiO_x, and HfO_x) became electron-conducting after an annealing in vacuum at temperatures ranging 400-600 °C. After thermal treatment, the valve metal nanostructures were suitable for Au electrodeposition on their tips (see Fig. 6(c,d). The methods described in this work offer the possibility to electrodeposit nanostructures anchored to a metal layer either directly through the concave cavities formed in the alumina barrier layer (the barrier-layer perforation) or indirectly through an array of the electron-conducting metal-oxide nanoprotrusions within the alumina barrier layer (the barrier-layer substitution). Electrochemical processes are also effective for modifying the morphology of the valve-metal oxide nanorods, transforming them into nanocavities or nanotubes (see Fig. 6(e–h). These hollow nanostructures were obtained through a reanodization step, where ionic transport processes between valve metal, alumina template and electrolyte, the local increase in temperature and the concentration of the electrolyte are the responsible factors of the modification of the morphology [139].

After the anodization process, an etching step may be applied to widen the pores and thin the barrier layer. One of the most common strategies to achieve this is chemical etching, usually by immersing the UTAM in 5% H_3PO_4 in water. Although this process has been explored for the complete removal of the barrier layer [80,136], it has shown to be inadequate in some cases due to the inherent anisotropy of the etching, which produces the complete dissolution of the pore walls prior to the barrier layer removal [116]. An alternative step consists of applying a reversal potential bias to dissolve the barrier layer, followed in some cases by chemical etching. The parameters required to remove the oxide barrier depend on the substrates and the presence of an interlayer. Zhao et al. reported a process to dissolve the barrier without disrupting the porous alumina structure, based on electrochemical etching in a neutral KCl solution using the UTAM as a cathode [101]. They also reported the electrochemical mechanism and its influence on the PAA membrane. Foremost, they performed a conventional two-step anodization. At the end of the second step, they reduced the voltage values to partially penetrate the barrier layer, forming fine-featured pathways while keeping a thin oxide layer at the pore bottom (see Fig. 7a). With the subsequent cathodic polarization of the sample, H_2O is decomposed into H^+ and OH^- at the cathode. The protons are attracted by the electric field, passing through the pathways where they reduce, forming H_2 that is immediately released from the surface of the alumina membrane. OH^- ions are generated at the bottom of each pore channel and are continuously transported to the anode. The presence of the OH^- ions can dissolve both the alumina barrier layer and the pore walls, following the next reactions:

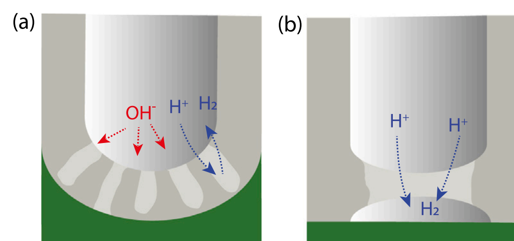

Fig. 7. Pore opening by cathodic polarization during the anodization process: (a) after anodization without reaching the interlayer material, (b) after reaching a conductive interlayer material.

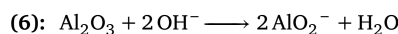

(6): $Al_2O_3 + 2\,OH^- \longrightarrow 2\,AlO_2{}^- + H_2O$

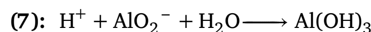

(7): $H^+ + AlO_2{}^- + H_2O \longrightarrow Al(OH)_3$

J. Oh and C. V. Thomson used a selective barrier perforation method based on the anodization of Al/W/Si thin films, followed by chemical etching of WO_3 using a pH 7 buffer solution (a mixture of sodium phosphate and potassium phosphate) [183]. N. Tasaltin et al. [135] reported the removal of the barrier layer of UTAM/Ti/SiO_2/Si substrate by cathodic polarization in KCl. The proposed mechanism for this latter approach is as follows: the cathodic bias produces protons that migrate toward the alumina barrier. These protons reach the interstitial voids and react, forming H_2 (see Fig. 7b). The hydrogen evolution, together with proton tunneling, produces an increase in pressure that results in localized alumina dissolution [116].

3. Attached UTAMs

In 1996, Masuda and Satoh proposed for the first time the use of UTAMs as masks to synthesize an array of nanodots, paving the way toward the utilization of UTAMs as templates for the fabrication of nanostructures [169,189]. The template was obtained by anodization and was subsequently detached from the remaining Al and transferred to the substrate, resulting in what is known as an attached UTAM. This method is very versatile and allows the use of nanoporous alumina templates to nano-pattern the surface of a substrate, similarly to using conventional lithography masks. It can be used in two different ways: by etching the surface of the sample that is uncovered by the template or by filling the pores. These processes are similar to those described in Fig. 1, but with the template transferred to the substrate instead of being prepared *in-situ*. This transfer method possesses several advantages compared with conventional nanolithography, particularly when dealing with nanostructures with dimensions lower than 100 nm (i.e., e-beam lithography). Specifically, e-beam lithography presents several drawbacks related to low throughput due to long exposure times and the lack of regularity of the obtained structure along the pore length. UTAMs can address both of these issues: due to their self-organized nanopore structure, large areas of ordered nanostructures can be synthesized in a relatively easy and low-cost process.

The use of attached UTAMs also presents some advantages over connected UTAMs. On one hand, the anodization process is not limited by the thickness of the aluminum. This fact opens the possibility to increase the first anodization time, which is responsible for the hexagonal order, thereby obtaining highly ordered nanopore arrays [35]. On the other hand, there is no interface between the Al substrate and the oxide membrane, allowing the pores to maintain their cylindrical morphology at the bottom. Finally, the alumina barrier layer at the pore bottom can be easily removed without exposing the pores to the etching agent, ensuring that they retain their original size and shape. Consequently, the pore widening can be more accurate, leading to high control of pore diameter. The main issue to consider is the transfer process: given the high brittleness of the thin PAA templates, the process of transferring them onto a substrate must be done carefully to avoid breaking the membrane. Many strategies for transferring the UTAMs to the substrates are proposed in the literature. In the following sections, the best results in UTAM transference are summarized.

3.1. Synthesis of alumina templates

In the case of attached UTAMs, the procedure for the synthesis of the templates is the conventional one, normally used for the preparation of freestanding PAA templates, which is well described in the literature [29,30,170]. In this section, the main characteristics of the procedure are summarized, with particular emphasis on the details connected with the fabrication of UTAMs.

The synthesis process starts with the cleaning and electropolishing of high-purity (∼ 99.999%) commercial Al foils. This pre-treatment plays an important role in the formation of the nanopores, as well as in the growth of the template [190]. In electropolishing, the roughness of the Al layer is reduced by removing undesired Al using electrochemical methods. Depending on the electropolishing parameters (time, voltage, electrolyte), a flat or a nanostructured surface can be obtained [191–194]. Prior to electropolishing, one might use thermal treatment to obtain better surface quality by removing mechanical stress and increasing the grain size. Normally, the annealing process is carried out at a temperature between 400 °C and 600 °C under an Ar atmosphere to avoid the oxidation of the aluminum [112,195–198].

Once the Al foils are cleaned and polished, they are ready for anodization. Two-step anodization is the most commonly used procedure to obtain well-ordered alumina templates. As discussed before, following this method, different pore diameters and interpore distances can be obtained depending on the anodization parameters (electrolyte, applied voltage, and temperature). The first anodization is longer than the second one because it is responsible for the nanopores' order in the template. The duration of the second anodization determines the final thickness of the membrane. For UTAMs, thickness usually ranges from a few hundred nanometers to 1-2 micrometers, and for this thickness, the time for the second anodization step is on the order of a few minutes. The temperature of the second anodization step can be reduced with respect to the first anodization to achieve more accurate control over the final thickness of the templates [70,195]. In addition to two-step anodization, one-step anodization procedures can be found in the literature: mild anodization [162,199] and hard anodization [179,200].

The mild anodization process is characterized by low applied voltages (25 V for sulfuric acid electrolytes [169], 40 V for oxalic acid electrolytes [137,167], and 195 V for phosphoric acid electrolytes [215]), low current densities (<10 mA/cm^2), and slow oxide growth rates (2-6 μm/h). In this self-ordered regime, the interpore distance (D_{int}) is linearly proportional to the anodization voltage [35], and common values of D_{int} are 65 nm for sulfuric acid, 110 nm for oxalic acid, and 500 nm for phosphoric acid.

Hard anodization offers the possibility to synthesize PAA with a wide range of interpore distances. It is characterized by higher applied voltages and low temperatures of the electrolyte (−10 to 0 °C). In particular, 40–70 V are used for sulfuric acid as the electrolyte [216], 140 V for oxalic acid [162], and 195 V for phosphoric acid [217], which lead to high current densities (in the range of 400–800 mA/cm^2). This anodization process does not occur in the self-order regime due to the high electric field exerted across the barrier layer, which is caused by the high current density. Consequently, there is no relation between D_{int} and the applied voltage. With hard anodization, it is possible to obtain interpore distances of 70–140 nm for sulfuric acid, 225–450 nm for oxalic acid, and 320–380 nm for phosphoric acid [218]. These interpore distances cannot be achieved with mild anodization. The main drawback of hard anodization for the synthesis of UTAMs is the high growth rates achieved during the anodization (10 times faster than for mild anodization), which makes it difficult to have precise control over the final thickness of the UTA. Due to this, although both mild and hard anodization are suitable for the synthesis of attached UTAMs, mild anodization is mostly used because of the lower growth rate of the aluminum oxide, allowing better control of the thickness of the alumina template. A combination of both anodization techniques can also be found, where a first hard anodization is carried out to create a pattern on the Al foil, and then mild anodization is used to obtain an ultra-thin alumina membrane. In this way, a small pore diameter combined with a large interpore distance can be achieved [219].

3.2. Transfer methods

The transfer of the UTAM to the substrate is the most important and delicate procedure in the synthesis process of attached UTAMs. It consists of detaching the membrane from the aluminum foil and transferring it to the substrate surface, with the challenge of guaranteeing the template's integrity. To achieve this objective, it is necessary to provide mechanical support to counteract the fragility of the ultra-thin membrane. This mechanical support can be provided by depositing a polymer on top of the UTAM (polymer-supported transfer) or by a wet transfer using a flat substrate. A diagram of the polymer-supported transfer is shown in Fig. 8. Once the UTAM is synthesized on top of the Al foil (1), the pores are filled with the polymer (2). Once the pores are completely filled and the template is coated, the Al foil is removed by chemical etching (3). If needed, the barrier layer at the bottom of the pores can also be removed (4). Afterward, the template is transferred to the substrate surface (5). Finally, the polymer is removed, leaving the pores of the template ready to grow the structure (6). Table 2 summarizes some of the most common procedures to transfer the UTAM.

Table 2
Summary of the substrates, polymers and procedures used in transfer UTAM applications. (VLS: Vapor Liquid Solid; RIE: Reactive Ion Etching; PVD: Physical Vapor Deposition; CVD: Chemical Vapor Deposition; ALD: Atomic Layer Deposition)

Substrate	Thickness of the PAA	Polymer	Barrier layer removal	Polymer removal	Transference method	Synthesis of the nanostructure	Ref.
Si	–	Nytrocellulose and Polyester	H_3PO_4	Acetone	Fishing with the substrate	e-beam evaporation	[169]
Si, GaAs, GaN	500 nm	–	H_3PO_4 and plasma etching	–	Directly after barrier layer removal	e-beam evaporation	[201]
Si	50-1000 nm	–	H_3PO_4	–	Plastic strainer	e-beam evaporation	[202]
Au-coated Si	300 nm	–	H_3PO_4	–	Van der Waals forces + 300 °C annealing (Ar)	Electrodeposition	[203]
Cu-coated Si	500 nm	–	H_3PO_4	–	Van der Waals forces + 500 °C annealing (Ar)	Electrodeposition	[204]
Si	<400 nm	PMMA (in anisole) and nail polish	H_3PO_4	Acetone	Directly after barrier layer removal	Chemical etching/ reactive ion etching	[195]
p-Si, glass, flexible polyimide	300 nm	PMMA (in anisole) and nail polish	H_3PO_4	UV-ozone after transfer	Thin acetone layer over the substrate	Atomic layer deposition	[70]
Si	<500 nm	Polystyrene	H_3PO_4	Imprinting under pressure	High pressure Ar stream	Vapor layer deposition	[205]
Si	80 nm	PMMA	H_3PO_4	Acetone under pressure	Thin acetone layer over the substrate	–	[112]
p-Si, glass, flexible polyimide	300 nm	Polystyrene	H_3PO_4	$CHCl_3$	Fishing with the substrate	Sputtering	[206]
Si, glass, flexible polyimide	300 nm	PMMA	H_3PO_4	UV-ozone in a dry stripper	Thin acetone layer over the substrate	ALD	[70]
$SrTiO_3$, MgO, LSAT, $LaAlO_3$	200 nm	–	Ar milling	–	Oxygen plasma and drop water	Sputtering VLS	[207]
Si, SiO_2, PMMA	1000 nm	–	H_3PO_4	–	PMMA	–	[208]
ITO-coated glass, Si, PET	<2000 nm	–	H_3PO_4	–	Plastic strainer	e-beam evaporation	[196]
p-Si	300-500 nm	–	H_3PO_4	–	Al foil and ion milling	e-beam evaporation etching	[209]
p-NiOx, FTO, ITO	<300 nm	Polystyrene	H_3PO_4	Chloroform	Fishing with the substrate	Evaporation	[197]
Si	<100 nm	PMMA	H_3PO_4	Acetone	Fishing with the substrate	e-beam evaporation	[198]
Si, Si/SiO_2, ITO	10-15 nm	PMMA	H_3PO_4	Annealing at 400 °C under N_2	Thin acetone layer over the substrate	e-beam evaporation	[210]
Si, quartz, MgO, LAO, STO	700 nm	S1813 and PMMA	H_3PO_4	Acetone and chloroform	Fishing	Electrodeposition	[211]
Teflon	1000 nm	Polystyrene	H_3PO_4	Toluene	Ethanol layer over the substrate	Argon based RIE/ oxygen plasma	[212]
Si	500 nm	PMMA	H_3PO_4	Oxygen dry etching	Fishing in ultrasounds bath	RIE dry etching	[213]
PET, FTO, Si, Curved glass, ITO …	<100 nm	PMMA	H_3PO_4	Acetone	Gas-flow assisted transfer	PVD	[214]
Quartz	200-500 nm	PMMA	H_3PO_4	Acetone	Fishing	Thermal evaporation	[65]
Si covered by diamond sheet	1600 nm	Silicone	H_3PO_4	Acetone	Liquid environment of acetone	CVD	[73]

The polymer used as supporting material for the transference of the UTAMs should be selected with care. It should be flexible, as well as mechanically and chemically stable. Furthermore, it should be liquid at room temperature which makes the filling process easier but also it must be easily removed from the template. Once the membrane is coated with the polymer, a dry process is carried out to produce solidification. In addition, polymers can be dissolved by organic compounds after the transfer process without leaving any residual material that could eventually block the pores. Among the different types, the most common polymers used in the literature for transferring UTAMs are polymethyl methacrylate (PMMA) [70,112,195,198,210,211,213,214] and polystyrene (PS) [197,205,206,212]. They are normally mixed with organic solvents (anisole, chlorobenzene, chloromethane, etc.) [70,112,195,197,198,206,211] to make the polymers more fluid and to ensure better filling. PMMA can be combined with other conventional photoresists to use it as supporting material. For example, S1813 provides chemical protection to the alumina pore walls due to the excellent filling of pores that is achieved and does not leave organic impurities within the pores, although it is quite fragile. In combination with PMMA, which provides the needed mechanical strength, it is possible to carry out the transfer process without any risk of breaking or leaving organic compounds inside the UTAM [211]. Spin coating or direct drop casting over one side of the UTAM are the most commonly used approaches to cover the alumina surface. After that, a dry process at room or higher temperatures (up to 120 °C) is necessary to evaporate the solvents and solidify the polymer [70,112,195]. The removal of the supporting material after anchoring the UTAM to the substrate is normally done by chemical etching with organic solvents like acetone, chloroform, or chloromethane [112,197,198,206,211]. Annealing [210] or photodegradation using UV light [70] can also be used in those cases where it is necessary to avoid the use of organic solvents.

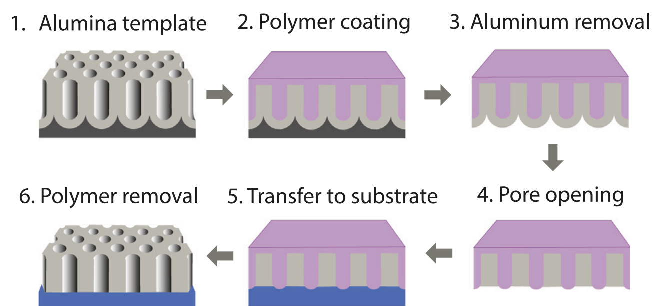

Fig. 8. Polymer-supported transfer process: (1) alumina template after anodization process, (2) polymer coating, (3) aluminum removal, (4) pore opening, (5) transfer to substrate and (6) polymer removal.

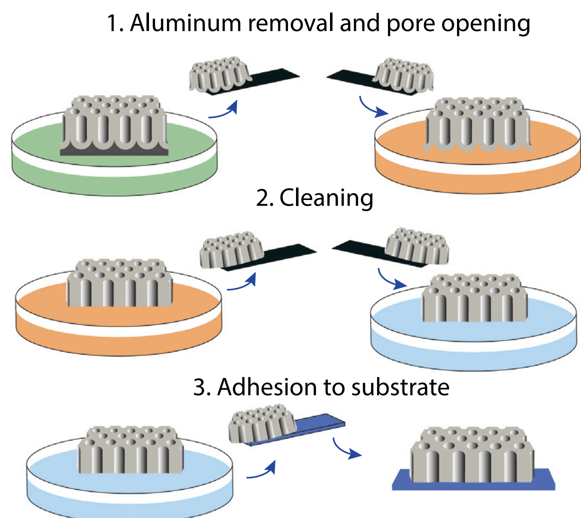

Fig. 9. Description of wet transfer process of UTAMs.

In some cases, the transfer processes can be carried out without using polymer-support. For that, the alumina template is detached from the Al foil and remains freestanding until it is placed over the substrate surface. To manipulate these free UTAMs, a plastic strainer or a flat substrate is normally used to *fish* the template from the solutions to the sample surface [196,198,201,202]. Fig. 9 illustrates the process of the Al removal and pore opening of a UTAM without any supporting material. The membrane is kept floating on the different etching solutions and, in the end, is *fished* to be transferred onto the substrate.

The first step in this procedure is to remove the excess of Al by chemical etching with a solution of HCl and $CuCl_2$. The most important part of this process is to keep the sample floating on the solution, avoiding its sinking to prevent pore contamination with solution agents and copper–aluminum waste that precipitates during the Al etching (Fig. 9.1 left). The next step is to transfer the alumina to the next container with the solution for alumina removal for pore opening by dissolving the oxide barrier layer (Fig. 9.1 right). Special care must be taken when transferring the sample from one solution to another. Rigid and flat surfaces, like glass slides or Si wafers, are used as supporting substrates to *fish* and deposit the membrane in the next solution. Plastic strainers are also useful due to their perforated surface, which helps the sample detach when introduced into new solutions. During the pore opening, the sample should also be kept floating on the solution. It is important to leave the sample floating with the barrier layer side in contact with the solution; otherwise, the pore walls will be dissolved before the barrier layer is removed. Once the pores are fully opened, the sample begins to sink. At this moment, the sample must be

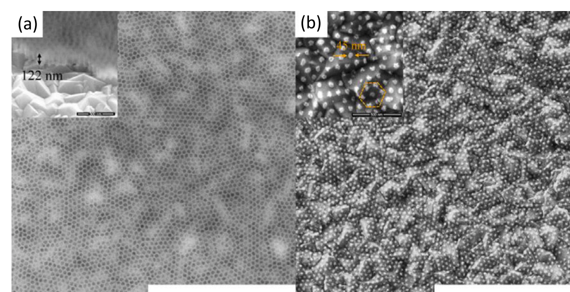

Fig. 10. (a) Plain-view and oblique-view SEM images of a 122 nm thick UTAM transferred to a rough FTO substrate (33 nm RMS). (b) Au nanodot array with sub−50 nm particle size fabricated by evaporating 10 nm Au through the UTAM mask onto FTO surface. Scale bars are 3 μm in both images. Adapted with permission from [197]. Copyright 2016 American Chemical Society.

transferred to the next container to prevent the etching solution from filling the alumina pores and to avoid pore widening. Once aluminum is removed and the pores are opened, a cleaning step is necessary before attaching the UTAM to the substrate surface. For that, the UTAM is transferred into a container with deionized water (Fig. 9.2). The transfer procedure is the same in all steps, except for the adhesion to the definitive substrate(Fig. 9.3). In this case, if the substrate can be immersed in water, the best option is to *fish* the UTAM with it and dry it at room temperature or through annealing. In cases where substrates cannot be immersed in water, the UTAMis *fished* with the supporting substrate (the same as in previous steps) and transferred to the definitive substrate, keeping the UTAM wet in acetone.

The possibility of leaving an Al frame in the UTAM [207] or even the Al foil [209] should be considered to facilitate the transfer process. It is important to take into account that when doing the transfer without a supporting layer, the pores of the UTAM are not protected with any kind of material; the pore walls are exposed to the etching agents, and the pore diameter might become widened. To avoid changing the pore size, plasma etching [201] or ion milling [209] can be used to remove the barrier layer in a more accurate way.

After completing the synthesis process and the pore opening, the UTAMs are transferred to the substrate surface. Good adherence must be achieved to ensure optimal performance of the alumina mask. The substrate surface must be as clean as possible to avoid the nucleation of air voids at the interface of the substrate and the UTAM. Chemical etching and plasma treatments are still effective in improving the surface properties and making it more active to create Van der Waals bonds between the UTAM and the underlayers [201,207,209]. Most authors drop some acetone or deionized water on the substrate before transferring to guarantee the adhesion of the membrane [112,207,209, 210]. Dry heating is also used to improve the adhesion of the alumina layer [203,204].

3.3. Capability and versatility in fabricating

The attached UTAMs offer great versatility in fabricating ordered nanostructures with a wide range of dimensions across several types of substrates, from flat substrates (i.e. silicon, GaAs, GaN, glass wafers, quartz), different oxides (MgO, LAO, STO, etc.), and polymers (i.e. PET, flexible polyimide) to rough substrates, even objects with complex morphologies like wires or curved samples [196,206,207]. The low thickness of UTAMs allows them to adapt and cover undulating surfaces [197]. In Fig. 10a, an example of an UTAM attached to the surface of an FTO substrate with a roughness of 33 nm (RMS) and approximately 200 nm peak-to-peak surface roughness is shown. Fig. 10b displays an array of Au nanodots resulting from the evaporation of 10 nm Au over the FTO surface after the removal of the alumina mask.

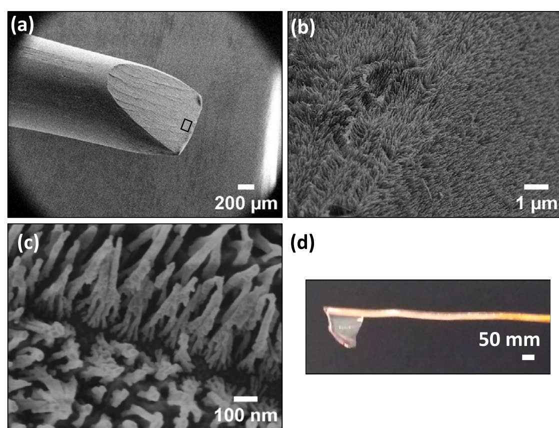

Fig. 11. SEM images of an Al rod coated with dendritic NWs. (a) View of the Al rod. (b) Zoom of the black square region of the rod in (a). (c) Detailed view of the dendritic NWs. (d) UTAM template attached to a Cu wire. Adapted with permission from [220].

Another example is nanostructuring curved surfaces. This is a challenging process that is difficult to achieve with conventional lithographic techniques or direct anodization of these surfaces due to low homogeneity and reproducibility. In Fig. 11a, an Al wire coated with Ni nanowires is presented [220]. In this process, the surface was anodized by modifying the anodization parameters to generate a dendritic structure [221], which allowed overcoming the oxide barrier layer to subsequently grow the Ni nanowires (Fig. 11b,c). However, at this point, the process does not yet provide completely homogeneous surfaces, and reproducibility is still limited. In contrast, anchoring the UTAMs to non-flat substrates can be advantageous, as shown by Guiliani et al. [211]. The authors were able to grow Ni nanowires by electrodeposition over the surface of a Cu nanowire using the attached UTAM as a template, in the same way as in Fig. 11d. The size of the Cu wire was on the same order as the lead of a mechanical pencil. The conductive wire was covered by a homogeneous pattern of Ni nanowires. This technique provides the opportunity to nanostructure curved surfaces, an approach that is very difficult to achieve with conventional lithographic techniques.

The good adhesion of the attached UTAMs to different kinds of substrates makes them suitable for a wide range of growth techniques to synthesize self-assembled nanostructures (see Table 2). These techniques range from physical depositions (PVD) (e-beam and sputtering) [112,196,206] and reactive ion etching (RIE) [195] to chemical routes where precursor liquids are put in contact with the alumina mask (i.e., electrodeposition, atomic layer deposition, and vapor–liquid–solid deposition) [70,203–205]. The capability to use this wide range of synthesis strategies broadens the field of application for attached UTAMs and makes them more versatile for patterning surfaces with different kinds of nanostructures, namely nanomeshes, nanodots, nanowires, nanopillars, and nanoholes.

The use of attached UTAMs is also very suitable for large-scale fabrication. The synthesis of UTAMs is scalable, allowing large sample areas to be covered with the alumina mask. This opens the possibility of using UTAMs in applications where a large nano-patterned surface is required. One example of the synthesis of large-area UTAMs is shown in the work developed by Meng et al. [207]. They present a successful methodology to fabricate uniform-sized nanowires at sub-lithographic scale on large-area substrates by using freestanding attached UTAMs. In Fig. 12, there are two examples of large-scale ultra-thin alumina templates with different shapes (circular and square), freestanding with an Al frame (left) and attached to a silicon wafer (right).

Regarding large-scale nano-patterning using UTAMs, one of the main disadvantages of using these membranes is the formation of wrinkles during the transfer process. As a solution to this problem,

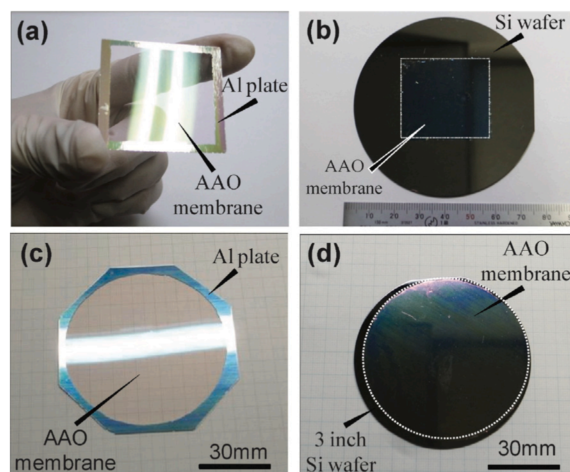

Fig. 12. (a) Square-type freestanding UTAM with 200 nm thickness and (b) the transferred membrane on the Si substrate. (c) Circle-type freestanding UTAM with 200 nm thickness and (d) the transferred membrane on the 3 inch Si wafer. Reproduced from Ref. [207] with permission from the Royal Society of Chemistry.

Zhang et al. [214] developed a method based on Gas-Flow-Assisted transfer to avoid the formation of voids at the interface between the substrate and the UTAM, successfully transferring the membranes onto arbitrary substrates, including curved ones. The proposed method allows for the transfer of large-scale UTAMs without showing wrinkles after adhesion to the substrate surface. As mentioned before, having wrinkle-free membranes attached to the substrate is crucial for UTAMs as masks for nano-patterning. The proposed method utilizes contact angle hysteresis to bulge the trapped droplet between the substrate and the UTAM, simultaneously stretching the UTAM during rapid dewetting driven by gas flow. This method has no durability concerns and does not alter the surface nature of the substrates, making it very versatile for nano-patterning large areas using alumina masks.

Another advantage of using attached UTAMs as masks is the ease of template removal without damaging the structure within the pores. Several techniques, such as chemical etching [203,211] and peel-off using adhesive tape [214,222,223], are employed to remove the alumina layer.

In addition, to reduce the fabrication costs and reduce the impact of the UTAM fabrication in the environment, Anh et al. [224] used aluminum cans as starting material for the fabrication of the UTAMs. The aluminum cans are one of the largest urban solid-waste. Previous to the anodization process, aluminum foils from cans were boiled in water and then treated in methyl ethyl ketone and acetone to remove label-painting layer. Followed by a common electropolish and anodization processes, authors obtained UTAMs with controllable pore size and thickness, in a cost-effective way, making PAA a potential hard-template for nanopatterning.

4. Nanostructures fabricated using UTAM nanopatterning

PAA templates have been used in the past and in the present in many technological areas, as they are an excellent tool for nanofabrication, mostly linked to the growth of electrodeposited nanowires [225,226] and, more recently, to more complex structures [60,61]. These nanoporous templates provide a cheap and easy route to fabricate homogeneous and ordered arrays that can be used not only as templates for nanofabrication but also as active or passive parts of optical [227] and electrical devices [29,228]. The reduction of the template thickness that UTAM provides, together with its excellent chemical [229,230] and mechanical stability [231], enlarges the potential applications of PAA membranes [232]. In addition, alumina is a biocompatible material [233–235], which opens the possibility of using UTAM-based devices as biosensors and biomaterials.

4.1. Magnetic nanostructures

The magnetic recording industry is one of the largest industries in the world, which has gained even greater interest due to the exponential growth of data production related to Big Data. For recording applications, achieving a large bit density in extensive areas is a must. The use of patterned media, in which each bit is lithographically predefined in the recording medium, has been explored as an alternative recording scheme [236–238]. The control that PAAs and UTAMs allows on pore diameter and distribution, as well as the possibility of patterning large areas, have been shown as an efficient way to control the magnetic properties of magnetic patterned media [239,240]. In fact, some efforts were made in the past to produce CoPt patterned media on Si using UTAMs as templates [124]. Recently, the use of UTAMs with a smoothed surface characterized by flattened interpore areas to produce large nanostructured surfaces of nanomagnets with perpendicular magnetic anisotropy has highlighted the importance of using UTAMs in recording devices [241]. With the emergence of 3D nanomagnetism [242] and novel spintronics solutions to data storage and processing problems [243], the combination of UTAMs and electrodeposition has been proposed to fabricate three-dimensional advanced devices such as Spin-Transfer-Torque oscillators [104,105,244].

4.2. Quantum dots and optical devices

UTAMs have been regularly used in recent years to produce nanopatterned structures on the surface of conventional semiconductors. For this purpose, the template is directly fabricated by anodization of evaporated Al on top of the semiconductor [85,245]. Afterward, the semiconductor surface is chemically etched using, in some cases, metallic particles as catalysts. This is a maskless lithography method that allows the fabrication of large nanostructured semiconductor areas in quantum-sized regime [112]. Using this procedure, InAs quantum dots can be fabricated over large GaAs areas [246]. On the other hand, large-scale arrays of nanoholes can be patterned in optical devices to improve their performance. An example of this is the work done by Zheng et al. [247], where large UTAM areas were used to create arrays of nanoholes on the GaN surface of a GaN-based LED. Nanopatterning the surface of the GaN increases the photoluminescence of the material by 3.4 times, as well as its efficiency. Furthermore, in this work, the authors developed a UTAM-based nanopatterning procedure compatible with mass production, which demonstrates the versatility of UTAMs as masks for nanostructuring surfaces.

As mentioned before, UTAMs can be used not only as templates for maskless lithography but also for the integration of nanostructures in different devices. Aluminum oxide exhibits excellent dielectric properties for the fabrication of optical devices in which nanostructuration is exploited [248]. UTAMs can tune the transparency and wettability of glass, opening the possibilities of creating self-cleaning and anti-frost glasses for buildings, vehicles, and other applications [249]. They also help to reduce the optical losses of Si-based optical devices. By appropriately tuning the anodization parameters, an UTAM grown on top of a Si device can increase the optical reflectance of the device from 40-50% of bare Si to less than 10% across a broad range of wavelengths and wide reflective angles [250]. The same idea has been explored to enhance the performance of GaAs-based solar cells, reducing the reflectance down to almost zero and thus increasing the theoretical performance of the device [251]. UTAMs have also been applied to introduce nanostructuration in other designs of solar cells. For example, UTAMs were used as templates for the growth of CdSe nanorods in TiO_2-based solar cells [146], demonstrating good photovoltaic activity for future integration in solar cells with superior performance characteristics. Another example is the use of UTAMs to create arrays of Au and CdS nanowires to achieve higher efficiency solar cells [86].

4.3. Plasmonics

UTAMs are useful for introducing ordered patterns in materials' surfaces. In the field of plasmonics, UTAMs offer a very efficient route to couple the induced periodicity with plasmon excitation, paving the way for the development of new applications. For example, it is possible to obtain ordered nanostructures with tunable optical properties, enhancing the electromagnetic response in molecular sensors [102,197,198,252,253]. Wurtz et al. studied coherent electromagnetic interactions of molecular plasmonics that affect the strength of the coupling between a plasmon and a molecular exciton [145]. This strength is highly affected by the spatial and spectral overlap between the plasmonic structure (in this case, Au nanorods) and the molecular aggregates. For this reason, by tuning the periodicity of the UTAMs, it is possible to control the optical properties of the grown nanorods.

Similarly, Au nanorods coated with VO_2 have been used to improve light absorption by combining plasmonic absorption with thermochromism [254]. Plasmonic-based Si solar cells coated with Ag nanoparticles can also be fabricated using UTAMs as templates, improving the conversion efficiency compared to reference solar cells [255].

Recent developments in Surface Enhanced Raman Scattering (SERS) sensors also incorporate UTAM technology. The Raman spectroscopy allows to capture molecular fingerprint information by detecting inelastic scattering of incident photons after the interaction with plasmonic nanostructures. The role of the UTAMs in these devices is to act as masks to create arrays of plasmonic nanostructures, typically Ag or Au nanoparticles [256,257], nanodots [253], nanorods [258,259], nanotubes [260,261] or nanocavities [262]. Both, *in-situ* anodized UTAMs and attached UTAMs approach are used in the fabrication of SERS. SERS-based sensors are intensively used as biological and chemical sensors [263] due to its cost-effective fabrication and non-invasive performance.

4.4. Energy applications

Nanostructured materials containing UTAMs have also promising applications in the field of green energies. In most energy applications, device performance scales with the active surface area. Therefore, nanostructuring the surface of the active regions of devices may enhance their functional properties. For example, in the case of photoanodes for water splitting, nanorods with a large aspect ratio are more effective than smaller nanorods or thin films [264].

Supercapacitors are crucial components in renewable energy technologies, helping to smooth intermittent energy generation in solar and wind power systems, as well as enhancing the efficiency of electric vehicles, among other applications [265,266]. Nanomaterials [267], particularly template-based materials [268], are promising candidates for the development of advanced supercapacitors with enhanced properties. In this context, various approaches are being explored to create high-performance capacitors using UTAMs. For instance, a two-step anodization process on Al/W/Ti-coated Si substrates has been used to prepare vertically oriented tungsten oxide nanorods. The nanostructured surface exhibits pseudocapacitive behavior, high specific capacitance and cyclability [269]. The active surface area of a material can also be increased by evaporating a thin film onto a UTAM, which coats the pores, forming a continuous 3D nanofilm. This method has been employed to prepare Ta–Nb alloy/oxide coatings, which can serve as novel 3D nanostructured electrodes/dielectrics for electrolytic microcapacitors, suitable for traditional electronic circuits and energy storage applications [270]. This strategy of creating 3D nanofilms with increased surface area has also been applied to the preparation of gas sensors, where enhancing the active surface area improves performance [271].

4.5. Biomedical applications

The biocompatibility of aluminum oxide, together with the potential for nanostructuring surfaces below the micrometer region (i.e., the size of human cells and neurons), is currently increasing the potential use of PAA in general, and UTAMs in particular, in the development of neural interfaces [53] and other biomedical devices [272]. On one hand, the excellent mechanical properties of PAA have been exploited to improve the mechanical properties and bioactivity, as well as to enhance the adhesion between bone and Ti-based (Ti–6Al–4V) implants [92]. For that, the authors prepared a PAA coating on top of the Ti alloy by anodizing an Al layer, which was previously evaporated. Titania pillars have also been synthesized using PAA to study the influence of the nanopillar height on cell adhesion, spreading, cytoskeletal formation, and differentiation, as they are sensitive to the topography [273]. On the other hand, the nanostructure provided by the use of PAA improves cell adhesion in cell cultures [91,187,274–277]. This adhesion can be further exploited to develop devices that act as living cell biosensors for single-cell sensing [278].

Related to the development of biosensors, Zulfa et al. fabricated ZnO/Au nanosquare-array electrodes to detect the concentration of glucose related to diabetes mellitus [279]. They combined zinc oxide (ZnO), due to its stability and low price, with Au nanoparticles to increase the electrode conductivity and to accelerate the oxidation of glucose. To fabricate these ZnO nanostructures, they stamped the Al surface with a Ni mold and anodized the Al surface, generating the porous structure. Afterward, they used PMMA to transfer the structure to a fluorine-doped tin oxide (FTO) substrate containing an Au layer. Finally, ZnO was deposited by DC sputtering into the porous structure, and the UTAM was removed. As a result, an array of ZnO nanosquares on top of an Au layer was obtained, which was explored to study their application as glucose biosensors and to determine their conductivity and optical properties. UTAMs can also be used as DNA sensing electrodes. In the work developed by S. A. Shamsuddin et al. [280], the authors functionalized the surface of the UTAMs to fix the DNA molecules onto the oxide surface. To sense the concentration of DNA, they measured the impedimetric response curve of the UTAM electrode. With this study, they demonstrated the good sensitivity and specificity of UTAMs in detecting different DNA compounds.

5. Conclusions and outlook

In conclusion, the anodization process of aluminum foils, which underpins the synthesis of porous anodic alumina oxide (PAA), has been explored with a focus on its applications in ultra-thin alumina membranes (UTAMs). Two main approaches to UTAM fabrication have been discussed: *in-situ* anodization of ultra-thin aluminum films deposited on various substrates, and the preparation of free-standing UTAMs with subsequent transfer to desired substrates.

In-situ anodization refers to the UTAMs produced by the anodization of ultra-thin Al layers directly grown on top of the surface to be nanostructured. In this case, significant attention has been given to substrate and buffer layer selection, growth conditions, and the structural and morphological properties of the aluminum layer, emphasizing how these parameters influence pore size, shape, and spacing. In the case of attached UTAMs, the nanoporous alumina template is normally prepared by conventional anodization procedures, extensively covered in other reviews. Various transfer techniques and their integration with physical and chemical methods for nanostructure synthesis have been highlighted. The versatility of UTAMs in fabricating diverse nanomaterials and tailoring their properties has been underscored, demonstrating their broad impact on advancing applications in information technology, renewable energy, and biomedical technologies.

Each approach has specific advantages that make it ideal for certain applications. When nanopatterning is required only in specific areas of the sample, *in-situ* anodization is the most suitable approach, particularly when combined with the lithography process to previously select areas for the patterning. In addition, *in-situ* anodized alumina templates are grown directly on top of the substrate surface without the need for a transference process, which minimizes the risk of cracking and/or contaminating the pores with supporting material. When nanopatterning large areas or surfaces with curvature – undulated or needled-shaped substrates – the attached UTAMs'approach is really beneficial.

The quality of the nanostructured area is also important for applications. *In-situ* nanoporous templates are obtained from the anodization of previously deposited Al thin films using PVD techniques, which sometimes increase surface roughness. In most cases, these Al layers cannot be electropolished before anodization, which leads to an inhomogeneous pore size and distribution. On the other side, high-ordered nanopatterns can be obtained by using the attached UTAMs' approach. In this case, the distribution of the pores, as well as the interpore distance and pore diameter, are easy to tailor. In general, the quality of alumina templates directly prepared on the substrates in terms of homogeneity of pore diameter and pore distribution is lower than that of transferred UTAMs.

Finally, in terms of costs, *in-situ* anodization requires higher investment for the fabrication of UTAMs as PVD techniques are required to cover the sample surface with high-purity aluminum whereas synthesizing the UTAMs from Al foils and further transfer to a substrate reduces the costs of their fabrication, as no specialized equipments are required.

To sum up, *in-situ* anodization is, in general, the most appropriate approach to follow when UTAMs are required in a specific region of the sample. When final applications require a high order distribution of the patterned nanostructures on the sample surface, a low distribution of pore diameter and interpore distance, or the surface of the substrate is curved, sharp or flexible, attached UTAMs would be the best choice.

Future research in UTAMs should focus on improving scalability and precision in fabrication techniques to enable mass production of high-quality, defect-free templates. Expanding applications to fields like nanomedicine or energy storage, the scalability requires, in addition, functionalizing UTAMs with specialized coatings or biomolecules. Developing advanced adhesion layers and interfacial materials will enhance compatibility with diverse substrates, including flexible and biocompatible materials. Efforts should prioritize refining control over pore size, shape, and distribution, for *in-situ* anodization. Sustainability is a critical challenge, necessitating eco-friendly anodization processes and recycling strategies since a major part of the reported works used high pure aluminum. Finally, low-cost approaches from the precursor aluminum foil or thin films to the techniques to grow nanostructures inside the nanopores will make UTAMs more accessible for industrial-scale applications.

Declaration of competing interest

The authors declare that they have no known competing financial interests or personal relationships that could have appeared to influence the work reported in this paper.

Acknowledgments

Funded by the European Union through project BEETHOVEN (101129912). Partially funded also by MCIN/AEI, Spain/10.13039/501100011033 through Projects PID2020-117024GB-C43, PID2022-141080OB-C22 and TED2021-130957B-C52. IMDEA Nanociencia acknowledges support from the Severo Ochoa Programme for Centres of Excellence in R&D, Spain (Grant SEV-2016-0686). A. A.-N. and S. R.-G. acknowledge funding through the Advanced Materials programme supported by MCIN with funding from the European Union NextGenerationEU (PRTR-C17.I1) and by the Generalitat de Catalunya, Spain. C.T.S. acknowledges the program Atraccion de Talento (CAM), ref. 2020-T1/IND-19889. Views and opinions expressed are however those of the authors only and do not necessarily reflect those of the European Union or the other granting authorities. Neither the European Union nor the granting authorities can be held responsible for them.

Data availability

No data was used for the research described in the article.

References

[1] J.A. Rogers, H.H. Lee, John Wiley & Sons, Inc., 2009.
[2] A. Elmekawy, E. Iashina, I. Dubitskiy, S. Sotnichuk, I. Bozhev, D. Kozlov, K. Napolskii, D. Menzel, A. Mistonov, J. Magn. Magn. Mater. 532 (2021) 167951.
[3] C. Fernández-González, A. Berja, L. Álvaro-Gómez, C. Martín-Rubio, A. Mascaraque, L. Aballe, R. Sanz, L. Pérez, S. Ruiz-Gómez, Scr. Mater. 243 (2024) 115970.
[4] M. Salaheldeen, V. Vega, A. Ibabe, M. Jaafar, A. Asenjo, A. Fernandez, V.M. Prida, Nanomaterials 8 (2018) 227.
[5] M.-Y. Im, P. Fischer, K. Yamada, T. Sato, S. Kasai, Y. Nakatani, T. Ono, Nature Commun. 3 (2012) 983.
[6] K.J. Merazzo, C. Castán-Guerrero, J. Herrero-Albillos, F. Kronast, F. Bartolomé, J. Bartolomé, J. Sesé, R.P. del Real, L.M. García, M. Vázquez, Phys. Rev. B 85 (2012) 184427.
[7] I. Navarro-Baena, A. Jacobo-Martín, J.J. Hernández, J.R. Castro Smirnov, F. Viela, M.A. Monclús, M.R. Osorio, J.M. Molina-Aldareguia, I. Rodríguez, Nanoscale 10 (2018) 15496–15504.
[8] P. Pip, C. Donnelly, M. Döbeli, C. Gunderson, L.J. Heyderman, L. Philippe, Small 16 (44) (2020) 2004099.
[9] L. Skoric, D. Sanz-Hernández, F. Meng, C. Donnelly, S. Merino-Aceituno, A. Fernández-Pacheco, Nano Lett. 20 (1) (2020) 184–191.
[10] E. Berganza, E. Boltynjuk, G. Mathew, F.F. Vallejo, R. Gröger, T. Scherer, S. Sekula-Neuner, M. Hirtz, Small 19 (2023) 2205590.
[11] H.-N. Barad, H. Kwon, M. Alarcón-Correa, P. Fischer, ACS Nano 15 (2021) 5861–5875.
[12] A. Biswas, I.S. Bayer, A.S. Biris, T. Wang, E. Dervishi, F. Faupel, Adv. Colloid Interface Sci. 170 (2012) 2–27.
[13] J.M. De Teresa (Ed.), Nanofabrication. Nanolithography Techniques and Their Applications, IOP Publishing, 2020.
[14] N. Qin, Z.-G. Qian, C. Zhou, X.-X. Xia, T.H. Tao, Nature Commun. 12 (2021) 5133.
[15] A.S. Gangnaik, Y.M. Georgiev, J.D. Holmes, Chem. Mater. 29 (2017) 1898–1917.
[16] J.M. de Teresa, P. Orús, R. Córdoba, P. Pillipp, Micromachines 21 (2019) 799.
[17] J.R. Maldonado, M. Peckerar, Microelectron. Eng. 161 (2016) 87–93.
[18] A.A. Tseng, A. Notargiacomo, T. Chen, J. Vac. Sci. Technol. B 23 (2005) 877–894.
[19] S. Talukder, B. Gogoi, P. Kumar, R. Pratap, R. Maoz, J. Sagiv, Mater. Today Proc. 18 (2019) 740.
[20] D. Liu, Q. Wang, J. Hu, Appl. Surf. Sci. 356 (2015) 364–369.
[21] D. Navas, D.G. Trabada, M. Vázquez, Nanomaterials 11 (2021) 3430.
[22] E. Di Fabrizio, F. Romanato, S. Cabrini, F. Deangelis, A.A. Yu, R. Barsotti, G. Dealla Giustina, G. Brusatin, F. Stellacci, MRS Online Proc. Lib. 921 (2011).
[23] A. Matsuda, G. Kawamura, in: L. Klein, M. Aparicio, A. Jitianu (Eds.), Handbook of Sol-Gel Science and Technology, Springer International Publishing, 2016.
[24] D.P. Goronzy, M. Ebrahimi, F. Rosei, Arramel, Y. Fang, S.D. Feyter, S.L. Tait, C. Wang, P.H. Beton, A.T.S. Wee, P.S. Weiss, D.F. Perepichka, ACS Nano. 12 (2018) 7445–7481.
[25] T.R. Eaton, D.M. Torres, M. Buck, M. Mayor, Chimia 67 (2013) 222.
[26] K. Matczyszyn, J. Olesiak-Banska, J. Nanophotonics 6 (2012) 064505.
[27] N. Hannewald, P. Winterwerber, S. Zechel, D.Y.W. Ng, M.D. Hager, T. Weil, U.S. Schubert, Angew. Chem. Int. Edn 60 (2021) 6218–6229.
[28] Y. Lei, W. Cai, G. Wilde, Prog. Mater. Sci. 52 (2007) 465–539.
[29] A. Ruiz-Clavijo, O. Caballero-Calero, M. Martin-Gonzalez, Nanoscale 13 (2021) 2227.
[30] W. Lee, S.-J. Park, Chem. Rev. 114 (2014) 7487–7596.
[31] P.M. Resende, M. Martín-González, Micropor. Mesopor. Mat. 284 (2019) 311–316.
[32] J. Martín, C.V. Manzano, M. Martín-González, Micropor. Mesopor. Mat. 151 (2012) 311–316.
[33] J.T. Domagalski, E. Xifre-Perez, L. Marsal, Nanomaterials 11 (2021) 430.
[34] F. Arango, M. Sepúlveda, S. Aguilar-Sierra, F. Echeverría, Mat. Sci. Technol. 36 (2020) 1238–1244.
[35] K. Nielsch, J. Choi, K. Schwirn, R.B. Wehrspohn, U. Gosele, Nano Lett. 2 (2002) 677–680.
[36] L. Vojkuvka, L. Marsal, J. Pallarés, 2007 Spanish Conference of Electron Devices, 2007.
[37] M.M. Rahman, E. García-Caurel, A. Santos, L. Marsal, J. Pallarés, J. Ferré-Borrull, Nanoscale. Res. Lett. 7 (2012) 474.
[38] H. Han, S.-J. Park, J.S. Jang, H. Ryu, K.J. Kim, S. Baik, W. Lee, ACS Appl. Mater. Interfaces 5 (8) (2013) 3441–3448.
[39] S. Ruiz-Gómez, C. Fernández-González, L. Pérez, Micromachines 13 (2022) 1223.
[40] L. Piraux, Appl. Sci. 10 (5) (2020) 1832.
[41] V.M. Prida, V. Vega, J. Garcia, L. Iglesias, B. Hernando, I. Minguez-Bacho, Magnetic Nano- and Microwires: Design, Synthesis, Properties and Applications, Elsevier, Amsterdam, 2015.
[42] M. Vazquez, J. Magn. Magn. Mater. 543 (2022) 168634.
[43] M. Varga, L. Galdun, B. Kunca, V. Vega, J. García, V. Prida, E. Barriga-Castro, C. Luna, P. Diko, K. Saksl, R. Varga, J. Alloys. Compd. 897 (2022) 163211.
[44] M.T. Rahman, N.N. Shams, D.S. Wang, C.-H. Lai, Appl. Phys. Lett. 94 (2009) 082503.
[45] M. Salaheldeen, A.M. Abu-Dief, L. Martínez-Goyeneche, S.O. Alzahrani, P.Á.-A. Fatmah Alkhatib, J.Á. Blanco., Materials 13 (2020) 5788.
[46] W.J. Gong, W. Liu, J.N. Feng, D.S. Kim, C.J. Choi, Z.D. Zhang, J. Appl. Phys. 115 (2014) 133909.
[47] D.R. Saldanha, D.A. Dugato, T.J.A. Mori, N.F. Daudt, L.S. Dorneles, J.C. Denardin, J. Phys. D: Appl. Phys. 51 (2018) 395001.
[48] M. Salaheldeen, V. Vega, R. Caballero-Flores, V. Prida, A. Fernández, Nanotechnology 30 (45) (2019) 455703.
[49] E. Davoodi, M. Zhianmanesh, H. Montazerian, A.S. Milani, M. Hoorfar, J. Mater. Sci Mater. Med. 31 (2020) 60.
[50] A. Thormann, N. Teuscher, M. Pfannmöller, U. Rothe, A. Heilmann, Small 3 (6) (2007) 1032–1040.
[51] M. Martín-González, O. Caballero-Calero, P. Díaz-Chao, Renew. Sust. Energ. Rev. 24 (2013) 288–305.
[52] C.H. Huang, X.H. Sun, Y.H. Sun, Adv. Mater. Res. 399 (2012) 641–645.
[53] A. Domínguez-Bajo, J.M. Rosa, A. González-Mayorga, B.L. Rodilla, A. Arch'e-Núñez, E. Benayas, P. Ocón, L. Pérez, J. Camarero, R. Miranda, M.T. González, J. Aguilar, E. López-Dolado, M. Serrano, Biomaterials 279 (2021) 121186.
[54] Y.P. Ivanov, A. Alfadhel, M. Alnassar, J.E. Perez, M. Vazquez, A. Chuvilin, J. Kosel, Sci. Rep. 6 (2016) 24189.
[55] C.T. Sousa, A. Apolinario, D.C. Leitao, A.M. Pereira, J. Ventura, J.P. Araujo, J. Mat. Chem. 22 (2012) 6.
[56] D. Losic, L.V. Leonara, K. Kant, T. Kumeria, K. Gulati, J.G. Shapter, D.A. Beattie, S. Simovic, Aust. J. Chem. 64 (2011) 294–301.
[57] J. García, M. Méndez, S. González, V. Vega, R. Caballero, V.M. Prida, in: M. Vázquez (Ed.), Magnetic Nano- and Microwires, second ed., Woodhead Publishing, 2020, pp. 21–60.
[58] R. Xu, Z. Zeng, Y. Lei, Nature Commun. 13 (1) (2022) 2435.
[59] G. Meng, Y.J. Jung, A. Cao, R. Vajtai, P.M. Ajayan, Proc. Natl. Acad. Sci. USA 102 (2005) 7074–7078.
[60] J. Martín, M. Martín-González, J.F. Fernández, O. Caballero-Calero, Nature Commun. 5 (2014) 5130.
[61] A. Ruiz-Clavijo, S. Ruiz-Gomez, O. Caballero-Calero, L. Perez, M. Martin-Gonzalez, Phys. Status. Solidi. RLL 13 (2019) 1900263.
[62] A. Ruiz-Clavijo, O. Caballero-Calero, D. Navas, A.A. Ordoñez-Cencerrado, J. Blanco-Portals, F. Peiró, R. Sanz, M. Martín-González, Adv. Electron. Mater. 8 (2022) 2200342.
[63] C.V. Manzano, J. Rodríguez-Acevedo, O. Caballero-Calero, M. Martín-González, J. Mater. Chem. 10 (2022) 1787–1797.
[64] M.S. Sander, L.-S. Tan, Adv. Funct. Mater. 13 (2003) 393.
[65] Y. Wang, Y. Wang, H. Wang, X. Wang, M. Cong, W. Xu, S. Xu, Nanotechnology 27 (2) (2015) 025302.
[66] P.-L. Chen, C.-T. Kuo, T.-G. Tsai, B.-W. Wu, C.-C. Hsu, F.-M. Pan, Appl. Phys. Lett. 82 (2003) 2796.
[67] C.-L. Xu, H. Li, G.-Y. Zhao, H.-L. Li, Appl. Surf. Sci. 253 (2006) 1399–1403.
[68] S.-Z. Chu, K. Wada, S. Inoue, S. ichi Todoroki, Y.K. Takahashi, K. Hono, Chem. Mater. 14 (2002) 4595–4602.
[69] D. Wang, L. Zhang, W. Lee, M. Knez, L. Liu, Small 9 (7) (2013) 1025–1029.
[70] L.K. Tan, M.A.S. Chong, H. Gao, J. Phys. Chem. C 112 (2008) 69–73.
[71] R. Imai, M. Tanaka, H. Hashimoto, H. Asoh, Nanotechnology 31 (41) (2020) 415303.
[72] Y. Lei, S. Yang, M. Wu, G. Wilde, Chem. Soc. Rev. 40 (3) (2011) 1247–1258.
[73] C. Zhang, Z. Liu, C. Li, J. Cao, J.G. Buijnsters, Nanomaterials 13 (5) (2023) 888.
[74] K.P. Musselman, G.J. Mulholland, A.P. Robinson, L. Schmidt-Mende, J.L. MacManus-Driscoll, Adv. Mater. 20 (2008) 4470–4475.
[75] T.S. Kustandi, W.W. Loh, H. Gao, H.Y. Low, ACS Nano 4 (5) (2010) 2561–2568.
[76] K.M. Chahrour, N.M. Ahmed, M.R. Hashim, N.G. Elfadill, M. Bououdina, Sensors Actuators A 239 (2016) 209–219.
[77] P. Alonso-González, M.S. Martín-González, J. Martín-Sánchez, Y. González, L. González, J. Cryst. Growth 294 (2006) 168–173.
[78] S. Mátefi-Tempfli, M. Mátefi-Tempfli, Adv. Mater. 21 (2009) 4005–4010.
[79] S. Taheriniya, S.S. Parhizgar, A.H. Sari, Results Phys. 9 (2018) 1428–1435.
[80] D. Crouse, Y.-H. Lo, A.E. Miller, M. Crouse, Appl. Phys. Lett. 76 (2000) 49.
[81] D. Bruggemann, B. Wolfrum, V. Maybeck, Y. Mourzina, M. Jansen, A. Offenhausser, Nanotechnol. 22 (2011) 265104.
[82] A. Cai, H. Zhang, H. Hua, Z. Zhang, Nanotechnol. 13 (2002) 627–630.

[83] S.-K. Hwang, J. Lee, S.-H. Jeong, P.-S. Lee, K.-H. Lee, Nanotechnology 2005 (2005) 850–858.
[84] T. Shimizu, K. Aoki, Y. Tanaka, T. Terui, S. Shingubara, Japan. J. Appl. Phys. 50 (2011) 06GE01.
[85] H. Asoh, K. Fujihara, S. Ono, Nanoscale Res. Lett. 8 (2013) 410.
[86] S. Guduru, V.P. Singh, S. Rajaputra, S. Mishra, R. Mangu, Ingrid St. Omer, Thin Solid Films 518 (2010) 1809–1814.
[87] M.-P. Houng, W.-L. Lu, T.-H. Yang, K.-W. Lee, J. Nanomater. 2014 (2014) 130716.
[88] J.Y. Kim, K. Zhu, N.R. Neale, A.J. Frank, Nano Convergence 1 (2014) 9.
[89] R.E. Treharne, RF Magnetron Sputtering of Transparent Conducting Oxides and CdTe/CdS Solar Cells (Ph.D. thesis), Durham University, 2011.
[90] Z. Wang, C. Chen, K. Wu, H. Chong, H. Ye, Phys. Status Solidi A 216 (2019) 1700794.
[91] C. Toccafondi, S. Thorat, R.L. Rocca, A. Scarpellini, M. Salerno, S. Dante, G. Das, J. Mater. Sci Mater. Med. 25 (2014) 2411–2420.
[92] E.P. Briggs, A.R. Walpole, P.R. Wilshaw, M. Karlsson, E. Palsgard, J. Mater. Sci Mater. Med. 15 (2004) 1021–1029.
[93] K.L. Mittal, Electrocompon. Sci. Technol. 3 (1976) 21–42.
[94] A.A. Volinsky, N.R.M.W.W. Gerberich, Acta Mater. 50 (2002) 441–466.
[95] K.M. Chahrour, N.M. Ahmed, M.R. Hashim, N.G. Elfadill, A.M. Al-Diabat, M. Bououdina, J. Phys. Chem. Solids 87 (2015) 1–8.
[96] T.R.B. Foong, A. Sellinger, X. Hu, ACS Nano 2 (2008) 2250–2256.
[97] S.Z. Chu, K. Wada, S. Inoue, S. Todoroki, J. Electrochem. Soc. 149 (2002) B321–B327.
[98] M. Wu, I. Leu, M. Hon, J. Mater. Res. 19 (2004) 888–895.
[99] M.M. Crouse, A.E. Miller, D.T. Crouse, A.A. Ikram, J. Electrochem. Soc. 152 (2005) D167–D172.
[100] M. Tian, S. Xu, J. Wang, N. Kumar, E. Wertz, Q. Li, P.M. Campbell, M.H.W. Chan, T.E. Mallouk, Nano Lett. 5 (2005) 697–703.
[101] X. Zhao, S.-K. Seo, U.-J. Lee, K.-H. Lee, J. Electrochem. Soc. 154 (2007) C553–C557.
[102] S. Habouti, M. M'atéfi-Tempfli, C.-H. Solterbeck, M. Es-Souni, S. M'atéfi-Tempfli, M. Es-Souni, J. Mater. Chem. 21 (2011) 6269.
[103] K. Kim, M. Kim, S.M. Cho, Mat. Chem. Phys. 96 (2006) 278–282.
[104] F. Abreu Araujo, L. Piraux, V.A. Antohe, V. Cros, L. Gence, Appl. Phys. Lett. 102 (2013) 222402.
[105] L. Piraux, K. Renard, R. Guillemet, S. Mátéfi-Tempfli, M. Mátéfi-Tempfli, V.A. Antohe, S. Fusil, K. Bouzehouane, V. Cros, Nano Lett. 7 (2007) 2563–2567.
[106] N. Kwon, K. Kim, J. Heo, I. Chung, J. Nanosci. Nanotechnol. 14 (2014) 2885.
[107] S.-H. Jeong, H.-Y. Hwang, K.-H. Lee, Appl. Phys. Lett. 78 (2001) 2052–2054.
[108] A. Vlad, Advanced Fabrication of Nanowire Arrays and Three-Dimensional Nanostructures (Ph.D. thesis), Université Catholique de Louvain, 2009.
[109] P. Liu, V.P. Singh, S. Rajaputra, Nanotechnology 21 (2010) 115303.
[110] Y. Yanga, H. Chena, Y. Meib, J. Chena, X. Wub, X. Baob, Solid State Commun. 123 (2002) 279–282.
[111] T. Shimizu, M. Nagayanagi, T. Ishida, O. Sakata, T. Oku, H. Sakaue, T. Takahagi, S. Shingubarad, Electrochem. Solid. State. Lett. 9 (2006) J13–J16.
[112] M. Wu, L. Wen, Y. Lei, S.O.K. Chen, G. Wilde, Small 5 (2010) 695–699.
[113] M.M. Lohrengel, Mater. Sci. Eng. R Rep. 11 (1993) 243–294.
[114] D.-S. Tsai, C.-C. Chou, Metals 8 (2018) 105.
[115] C.A. Ross, J.S. Drewery, R.E. Somekh, J.E. Evetts, J. Appl. Phys. 66 (1989) 2349.
[116] N. Holubowitch, L. Nagle, J. Rohan, Solid State Ion. 216 (2012) 110–113.
[117] T.R.B. Foong, Y. Shen, X. Hu, A. Sellinger, Adv. Funct. Mater. 20 (2010) 1390–1396.
[118] O.-J. Lee, S.-K. Hwang, S.-H. Jeong, P.S. Lee, K.-H. Lee, Synth. Met. 518 (2010) 7283–7286.
[119] J. Mallet, K. Yu-Zhang, S. Mátéfi-Tempfli, M. Mátéfi-Tempfli, L. Piraux, J. Phys. D: Appl. Phys. 38 (2005) 909–914.
[120] S.W. Joo, A. Banerjee, Mat. Sci. Eng. B. 175 (2010) 36–40.
[121] A.I. Vorobjova, D.I. Tishkevich, E.A. Outkina, Y. Yao, I.U. Razanau, T.I. Zubar, A.A. Rotkovich, A.A. Bondaruk, M. Sayyed, S.V. Trukhanov, et al., Ceram. Int. 50 (22) (2024) 45703–45712.
[122] M.R. Maschmann, A.D. Franklin, P.B. Amama, D.N. Zakharov, E.A. Stach, T.D. Sands, T.S. Fisher, Nanotechnology 17 (15) (2006) 3925.
[123] Z. wei Zhang, J. Li, J. lei Liu, C. fei Zhu, Chin. J. Chem. Phys. 24 (2011) 115–120.
[124] A.I. Gapin, X.R. Ye, J.F. Aubuchon, L.H. Chen, Y.J. Tang, S. Jin, J. Appl. Phys. 99 (2006) 08G902.
[125] N.V. Myung, J. Lim, J.-P. Fleurial, M. Yun, W. West, D. Choi, Nanotechnology 15 (2004) 833?838.
[126] A.M. Abd-Elnaiema, A.M. Mebeda, W.J. Stępniowski, T. Czujkoe, Surf. Coat. Technol. 307 (2016) 359–365.
[127] K.M. Chahrour, N.M. Ahmed, M.R. Hashim, N.G. Elfadill, M.A. Qaeed, Appl. Phys. A 116 (2014) 1389–1393.
[128] K.M. Chahrour, N.M. Ahmed, M.R. Hashim, N.G. Elfadill, M.A. Qaeed, M. Bououdina, Superlattices Microstruct. 76 (2014) 197–204.
[129] D. Sanz-Hernández, C. Donnelly, L. Pérez, A. Fernández-Pacheco, in: V.K. Jain, A. Verma (Eds.), Physics of Semiconductor Devices, Springer International Publishing Switzerland, 2014.
[130] H. Shiraki, Y. Kimura, H. Ishii, S. Ono, K. Itaya, M. Niwano, Appl. Surf. Sci. 237 (2004) 369–373.
[131] X. Zhao, U.-J. Lee, S.-K. Seo, K.-H. Lee, Mat. Sci. Eng. C 29 (2009) 1156–1160.
[132] C.-L. Xu, S.-J. Bao, L.-B. Kong, H. Li, H.-L. Li, J. Solid State Chem. 179 (2006) 1351–1355.
[133] G.-Y. Zhao, C.-L. Xu, H.-L. Li, J. Power Sources 163 (2007) 1132–1136.
[134] J.-S. Jung, E.-M. Kim, W.-S. Chae, L.M. Malkinski, J.-H. Lim, C. O'Connor, J.-H. Jun, Bull. Korean Chem. Soc. 29 (2008) 2169.
[135] N. Tasaltin, S. Öztürk, N. Kilinc, H. Yüzer, Z.Z. Öztürk, Appl. Phys. A 95 (2009) 781–787.
[136] O. Rabin, P.R. Herz, Y.-M. Lin, A.I. Akinwande, S.B. Cronin, M.S. Dresselhaus, Adv. Funct. Mater. 13 (2003) 631.
[137] M.A. Kashi, A. Ramazani, J. Phys. D: Appl. Phys. 38 (14) (2005) 2396.
[138] A. Mozalev, J. Hubalek, Electrochim. Acta 297 (2019) 988–999.
[139] A. Mozalev, M. Bendova, F. Gispert-Guirado, Z. Pytlicek, E. Llobet, J. Mat. Chem. A 4 (21) (2016) 8219–8232.
[140] M. Es-Souni, S. Habouti, Front. Mater. 1 (2014) 19.
[141] S. Liu, Z. Xiong, C. Zhu, M. Li, M. Zheng, W. Shen, Nanoscale Res. Lett. 9 (2014) 159.
[142] C. Ottone, M. Laurenti, K. Bejtka, A. Sanginario, V. Cauda, J. Mater. Sci. Nanotechnol. 1 (2014) S107.
[143] J.J. Hill, K. Haller, K.J. Ziegler, J. Electrochem. Soc. 158 (2011) E1–E7.
[144] I. Voitovich, T. Lebyedyeva, A. Rachkov, O. Gorbatiuk, P. Shpylovyy, Nanoplasmonics, Nano-Optics, Nanocomposites and Surface Studies, Springer International Publishing Switzerland, 2015.
[145] G.A. Wurtz, P.R. Evans, W. Hendren, R. Atkinson, W. Dickson, R.J. Pollard, A.V. Zayats, Nano Lett. 7 (2007) 1297–1303.
[146] M. Schierhorn, S.W. Boettcher, S. Kraemer, G.D. Stucky, M. Moskovits, Nano Lett. 9 (2009) 3262–3267.
[147] L.-C. Chen, Chih-KaiWang, J.-B. Huang, L.-S. Hong, Nanotechnology 20 (2009) 085303.
[148] S.S. Shin, S.J. Lee, I. Seok, APL Mater. 7 (2019) 022401.
[149] B. Wang, W. Huang, L. Chi, M. Al-Hashimi, T.J. Marks, A. Facchetti, Chem. Rev. 118 (2018) 5690–5754.
[150] J.W. Schultze, M.M. Lohrengel, Electrochem. Acta. 45 (2000) 2499–2513.
[151] D. Matson, E. McClanahan, J. Rice, S. Lee, D. Windover, Surf. Coat. Technol. 133–134 (2000) 411–416.
[152] C.S. Whitman, J. Vac. Sci. Technol. B 18 (2000) 2842–2847.
[153] D.R. Lide (Ed.), CRC Handbook of Chemistry and Physics, CRC Press, Boca Raton, FL, 1995.
[154] C. Song-Zhu, K. Wada, S. Inoue, H. Segawa, J. Electrochem. Soc. 158 (2011) C148–C157.
[155] B.A. Movchan, A.V. Demchishin, Fiz. Metal. Metalloved 28 (1996) 653–660.
[156] P. Barna, M. Adamik, Thin Solid Films 317 (1998) 27–33.
[157] A.E. Lita, J.E. Sanchez Jr., Phys. Rev. B 61 (2000) 7692–7699.
[158] C.K. Chung, M.W. Liao, O.K. Khor, H.C. Chang, Thin Solid Films 544 (2013) 374–379.
[159] H. Takahashi, Y. Saito, M. Nakayama, J. Surf. Finish. Soc. Jpn. 33 (1982) 225.
[160] G.E. Thompson, Thin Solid Films 297 (1997) 192–201.
[161] G.E. Thompson, G.C. Wood, Nature 290 (1981) 230–232.
[162] W. Lee, R. Ji, U. Gösele, K. Nielsch, Nat. Mater. 5 (2006) 741–747.
[163] K. Shimizu, G.E. Thompson, G.C. Wood, Y. Xu, Thin Solid Films 88 (1982) 252–262.
[164] J.A. Davies, B. Domeij, J.P.S. Pringle, F. Brown, J. Electrochem. Soc. 112 (1965) 675–680.
[165] S.Z. Chu, K. Wada, S. Inoue, M. Isogai, Y. Katsuta, A. Yasumori, J. Electrochem. Soc. 153 (2006) B384.
[166] A. Mozalev, A. Surganov, S. Magaino, Electrochim. Acta 44 (1999) 3891–3898.
[167] F. Li, L. Zhang, R.M. Metzger, Chem. Mater. 10 (1998) 2470–2480.
[168] J.W. Diggle, T.C. Downie, C.W. Goulding, Chem. Rev. 69 (1969) 365–405.
[169] H. Masuda, M. Satoh, Japan. J. Appl. Phys. 35 (1996) L126.
[170] C.T. Sousa, D.C. Leitao, M.P. Proenca, J. Ventura, A.M. Pereira, J.P. Araujo, Appl. Phys. Rev. 1 (2014) 031102.
[171] F. Zhang, X. Liu1, C. Pan, J. Zhu, Nanotechnology 18 (2007) 345302.
[172] S. Ono, M. Saito, H. Asoh, Electrochim. Acta 5 (2005) 827–833.
[173] S. Liu, J. Tian, W. Zhang, Nanotechnology 32 (22) (2021) 222001.
[174] J.P. O'Sullivan, G.C. Wood, Proc. Roy. Soc. Lond. A 317 (1970) 511–543.
[175] V.P. Parkhutik, V.I. Shershulsky, J. Phys. D: Appl. Phys. 25 (1992) 1258.
[176] Q. Xu, G. Meng, F. Han, Prog. Mater. Sci. 95 (2018) 243–285.
[177] C.-J. Yang, S.-W. Liang, P.-W. Wu, C. Chen, J.-M. Shieh, Electrochem. Solid-State Lett. 10 (2007) C69–C71.
[178] P.G. Miney, P.E. Colavita, M.V. Schiza, R.J. Priore, F.G. Haibach, M.L. Myrickz, Electrochem. Solid-State Lett. 6 (2003) B42–B45.
[179] K. Schwirn, W. Lee, R. Hillebrand, M. Steinhart, K. Nielsch, U. Gösele, ACS Nano 2 (2008) 302–310.

[180] K.S. Choudhari, C.-H. Choi, S. Chidangil, S.D. George, Nanomaterials 12 (3) (2022) 444.
[181] H.-S. Seo, Y.-G. Jung, S.-W. Jee, J.M. Yang, J.-H. Lee, Scr. Mater. 57 (2007) 968–971.
[182] V. Khatko, A. Mozalev, G. Gorokh, D. Solovei, F. Guirado, E. Llobet, X. Correig, J. Electrochem. Soc. 155 (7) (2008) K116.
[183] J. Oh, C.V. Thompson, Adv. Mater. 20 (2008) 1368–1372.
[184] J. Oh, Y.C. Shin, C.V. Thompson, Electrochim. Acta 158 (2011) K11–K15.
[185] A. Mozalev, V. Khatko, C. Bittencourt, A.W. Hassel, G. Gorokh, E. Llobet, X. Correig, Chem. Mater. 20 (2008) 6482–6493.
[186] A.I. Vorobjova, D.I. Tishkevich, E.A. Outkina, D.L. Shimanovich, I.U. Razanau, T.I. Zubar, A.A. Bondaruk, E.K. Zheleznova, M. Dong, D.A. Aloraini, et al., Nanomaterials 12 (8) (2022) 1344.
[187] A.K. Eessaa, A. El-Shamy, Microelectron. Eng. (2023) 112061.
[188] A. Mozalev, M. Sakairi, H. Takahashi, J. Electrochem. Soc. 151 (11) (2004) F257.
[189] H. Masuda, K. Fukuda, Science 268 (5216) (1995) 1466–1468.
[190] J.M. Montero-Moreno, M. Sarret, C. Müller, Surf. Coat. Technol. 201 (2007) 6352–6357.
[191] A. Rauf, M. Mehmood, M.A. Rasheed, M. Aslam, J. Solid State Electrochem. 13 (2009) 321–332.
[192] D.C. Leitao, A. Apolinario, C.T. Sousa, J. Ventura, J.B. Sousa, M. Vazquez, J.P. Araujo, J. Phys. Chem. C 115 (2011) 8567–8572.
[193] D.C. Leitao, C.T. Sousa, J. Ventura, F. Carpinteiro, J.G. Correia, M.M. Amado, J.B. Sousa, J.P. Araujo, Phys. Stat. Sol. C 5 (2008) 3488–3491.
[194] V.V. Yuzhakov, H.C. Chang, A.E. Miller, Phys. Rev. B. 56 (1997) 12608–12624.
[195] H. Gao, N.N. Gosvami, J. Deng, L.-S. Tan, M.S. Sander, Langmuir 22 (2006) 8078–8082.
[196] Z. Zhan, Y. Lei, ACS Nano 8 (2014) 3862–3868.
[197] H. Robatjazi, S.M. Bahauddin, L.H. Macfarlan, S. Fu, I. Thomann, Chem. Mater. 28 (2016) 4546–4553.
[198] Q. Hao, H. Huang, X. Fan, X. Hou, Y. Yin, W. Li, L. Si, H. Nan, H. Wang, Y. Mei, T. Qiu, P.K. Chu, Nanotechnology 28 (2017) 105301.
[199] M.A. Kashi, A. Ramazani, M. Raoufi, A. Karimzadeh, Thin Solid Films 518 (2010) 6767–6772.
[200] L. Vojkuvka, J.F.-B. L.F. Marsal and, P. Formentin, J. Pallarés, Superlattices Microstruct. 44 (2007) 577–582.
[201] J. Liang, H. Chik, A. Yin, J. Xu, J. Appl. Phys. 91 (2002) 2544.
[202] G. Ding, M. Zheng, W. Xu, W. Shen, Nanotechnology 16 (8) (2005) 1285.
[203] I. Lombardi, P. Cavallotti, C. Carraro, R. Maboudian, Sensors Actuators B 125 (2007) 353–356.
[204] I. Lombardi, L. Magagnin, P.L. Cavallotti, C. Carraro, R. Maboudian, Electrochem. Solid-State Lett. 9 (2006) D13–D16.
[205] Z. Zhang, T. Shimizu, S. Senz, U. Gösele, Adv. Mater. 21 (27) (2009) 2824–2828.
[206] S.-H. Lyu, J.-S. Lee, J. Mater. Chem. 22 (5) (2012) 1852–1861.
[207] G. Meng, T. Yanagida, K. Nagashima, T. Yanagishita, M. Kanai, K. Oka, A. Klamchuen, S. Rahong, M. Horprathum, B. Xu, F. Zhuge, Y. He, H. Masuda, T. Kawai, RSC Adv. 2 (2012) 10618–10623.
[208] Z. Zeng, X. Huang, Z. Yin, H. Li, Y. Chen, H. Li, Q. Zhang, J. Ma, F. Boey, H. Zhang, Adv. Mater. 24 (2012) 4138–4142.
[209] A. Al-Haddad, Z. Zhan, C. Wang, S. Tarish, R. Vellacheria, Y. Lei, ACS Nano 9 (2015) 8584–8591.
[210] C. Zhao, Y. Zhu, L. Chen, S. Zhou, Y. Su, X. Ji, A. Chen, X. Gui, Z. Tang, Z. Liu, Nanoscale 10 (2018) 16278–16283.
[211] J. Guiliani, J. Cadena, C. Mo, Nanotechnology 29 (2018) 075301.
[212] S.K. Gopalakrishnan, M.A. Trujillo-Torres, C. Xu, K.J. Ziegler, ACS Appl. Eng. Mater. 1 (1) (2022) 616–627.
[213] T. Sun, F. Shui, X. Yang, Z. Zhou, R. Wan, Y. Liu, C. Qian, Z. Xu, H. Li, W. Guo, Nanomaterials 12 (11) (2022) 1875.
[214] H. Zhang, M. Zhou, Y. Guo, Z. Yu, R. Xu, L. Wen, Y. Wang, H. Zhao, Y. Lei, ACS Appl. Mater. Interfaces 13 (29) (2021) 35124–35132.
[215] H. Masuda, K. Yada, A. Osaka, Japan. J. Appl. Phys. 37 (11A) (1998) L1340.
[216] S.-Z. Chu, K. Wada, S. Inoue, M. Isogai, A. Yasumori, Adv. Mater. 17 (17) (2005) 2115–2119.
[217] Y. Li, M. Zheng, L. Ma, W. Shen, Nanotechnology 17 (20) (2006) 5101.
[218] Y. Li, M.J. Zheng, L. Ma, Appl. Phys. Lett. 91 (7) (2007) 073109.
[219] J. Liu, S. Liu, H. Zhou, C. Xie, Z. Huang, C. Fu, Y. Kuang, Thin Solid Films 552 (2014) 75–81.
[220] A. Arché Núñez, Fabrication, Characterization, and In-Vitro Biocompatibility of Nanowire-Based Neural Stimulation Electrodes (Ph.D. thesis), Universidad Complutense de Madrid, 2023.
[221] C.T. Sousa, D.C. Leitao, J. Ventura, P.B. Tavares, J.P. Araújo, Nanosc. Res. Lett. 7 (2012) 1–7.
[222] Z. Li, Q. Wan, J. Wang, G. Wang, Sci. Rep. 13 (1) (2023) 21939.
[223] Q. Gan, J. Yu, Y. Liao, W. Huang, G. Lin, J. Wang, J. Xu, C. Li, S. Chen, J. Zheng, Japan. J. Appl. Phys. 61 (7) (2022) 070902.
[224] D.H. Anh, N.Q. Toan, P.C.T. Tung, C.T. Son, H.P.T. Nguyen, H.-D. Nguyen, Vietnam J. Chem. 60 (1) (2022) 84–91.
[225] M. Stano, O. Fruchart, Handbook of Magnetic Materials, vol. 27, Elsevier, 2018.
[226] D. Sanz-Hernández, C. Donnelly, L. Pérez, A. Fernández-Pacheco, Nanofabrication. Nanolithography Techniques and their Applications, IOP Publishing, 2020.
[227] J. Dong, C. Li, Y. Wang, Y. Cao, Y. Fan, Q. Han, W. Gao, Y. Wang, J. Qi, Plasmonics 19 (2) (2024) 777–784.
[228] C.-A. Ku, C.-Y. Yu, C.-W. Hung, C.-K. Chung, Nanomaterials 13 (21) (2023) 2853.
[229] D.I. Petukhov, D.A. Buldakov, A.A. Tishkin, A.V. Lukashin, A.A. Eliseev, Beilstein J. Nanotechnol. 8 (1) (2017) 561–570.
[230] M. Iwai, T. Kikuchi, Thin Solid Films 771 (2023) 139784.
[231] J. Dai, J. Singh, N. Yamamoto, J. Am. Ceram. Soc. 101 (5) (2018) 2170–2180.
[232] K. Kamnev, M. Bendova, Z. Pytlicek, J. Prasek, L. Kejík, F. Güell, E. Llobet, A. Mozalev, Ceram. Int. 49 (22, Part A) (2023) 34712–34725.
[233] K.E. La Flamme, K.C. Popat, L. Leoni, E. Markiewicz, T.J. La Tempa, B.B. Roman, C.A. Grimes, T.A. Desai, Biomaterials 28 (16) (2007) 2638–2645.
[234] G. Poinern, X. Le, C. Loomes, D. Fawcett, Mater. Lett. 131 (2014) 182–185.
[235] K. Noh, K.S. Brammer, C. Choi, S.H. Kim, C.J. Frandsen, S. Jin, et al., J. Biomater. Nanobiotechnol. 2 (03) (2011) 226.
[236] A. Moser, K. Takano, D.T. Margulies, M. Albrecht, Y. Sonobe, Y. Ikeda, S. Sun, E.E. Fullerton, J. Phys. D: Appl. Phys. 35 (2002) R15.
[237] P. Chowdhury, S.B. Sellarajan, M. Krishnan, H.C. Barshilia, AIP Conf. Proc. 1447 (2012) 357–358.
[238] B. Sellarajan, P. Saravanan, S. Ghosh, H. Nagaraja, H.C. Barshilia, P. Chowdhury, J. Magn. Magn. Mater. 451 (2018) 51–56.
[239] M. Salaheldeen, V. Vega, A. Fernández, V. Prida, J. Magn. Magn. Mater. 491 (2019) 165572.
[240] M. Salaheldeen, M. Méndez, V. Vega, A. Fernández, V.M. Prida, ACS Appl. Nano. Mater. 2 (4) (2019) 1866–1875.
[241] T. Anh Nguyen, J. Fedotova, J. Kasiuk, V. Bayev, O. Kupreeva, S. Lazarouk, D. Manh, D. Vu, S. Chung, J. Akerman, V. Altynov, A. Maximenko, Appl. Surf. Sci. 427 (2018) 649–655.
[242] A. Fernandez-Pacheco, R. Streubel, O. Fruchart, R. Hertel, P. Fischer, R.P. Cowburn, Nat. Commun. 8 (2017) 15756.
[243] S.S.P. Parkin, M. Hayashi, L. Thomas, Science 320 (2008) 190–194.
[244] F. Abreu Araujo, L. Piraux, Spin 7 (2017) 1740007.
[245] H. Asoh, M. Matsuo, M. Yoshihama, S. Ono, Appl. Phys. Lett. 83 (2013) 4408.
[246] K. Meneou, C.L. Tsai, Z.H. Zhang, K.Y. Chenga, J. Vac. Sci. Technol. B 23 (2005) 1232–1236.
[247] X. Zheng, R. Jiang, X. Qu, Q. Li, F. Zeng, W. Wang, Z. Dai, Z. Xu, J. Peng, Z. Xu, Nanotechnology 31 (19) (2020) 195301.
[248] H.N.Q. Tran, K.N. Tran, S. Gunenthiran, J. Wang, C.S. Law, S.Y. Lim, Y.C. Gary Lim, A.D. Abell, L.F. Marsal, A. Santos, ACS Appl. Mater. Interfaces 16 (2024) 11787–11799.
[249] S. Lee, W. Kim, S. Lee, S. Shim, D. Choi, Scr. Mater. 104 (2015) 29–32.
[250] B. Dudem, J.W. Leem, M. Choi, J.S. Yu, Appl. Phys. B 118 (2015) 439–447.
[251] T. Yang, X. Wang, W. Liu, Y. Shi, F. Yang, Opt. Exp. 21 (2013) 18207.
[252] Y. Zhao, J. Xu, C. Feng, Y. Yan, J. Mater. Sci. 53 (2018) 16122–16131.
[253] Q. Hao, H. Huang, X. Fan, Y. Yin, J. Wang, W. Li, T. Qiu, L. Ma, P.K. Chu, O.G. Schmidt, ACS Appl. Mater. Interf. 9 (41) (2017) 36199–36205.
[254] S. Habouti, M. Es-Souni, Cryst. Eng. Comm. 16 (15) (2014) 3068–3071.
[255] W.-J. Ho, P.-Y. Cheng, K.-Y. Hsiao, Appl. Surf. Sci. 354 (2015) 25–30.
[256] M. Aguilar-Pujol, R. Ramírez-Jiménez, E. Xifre-Perez, S. Cortijo-Campos, J. Bartolomé, L.F. Marsal, A. de Andrés, Nanomaterials 10 (5) (2020) 830.
[257] K. Li, X. Tang, H. Wang, M. Huang, G. Liu, Y. Zhou, W. Huang, Z. Zuo, Y. Lu, Appl. Surf. Sci. 613 (2023) 156117.
[258] A.N. Kim, H. Lim, H.N. Lee, Y.M. Park, B. Yoo, H.-J. Kim, Appl. Surf. Sci. 446 (2018) 114–121.
[259] P. Pellacani, C. Morasso, S. Picciolini, D. Gallach, L. Fornasari, F. Marabelli, M. Manso Silvan, Materials 13 (5) (2020) http://dx.doi.org/10.3390/ma13051244, URL https://www.mdpi.com/1996-1944/13/5/1244.
[260] K. Sun, Q. Deng, H. Tang, Sustainability 14 (3) (2022) 1305.
[261] Y.-X. Yang, J.P. Chu, Nanotechnology 32 (47) (2021) 475504.
[262] S.M. Lee, D.H. Nam, D. Lee, S.H. Lim, S.J. Son, S. Lee, ACS Appl. Nano Mater. 4 (12) (2021) 12905–12912.
[263] Z. Wu, M. Sha, D. Ji, H. Zhao, L. Li, Y. Lei, ACS Appl. Nano Mater. 7 (1) (2024) 11–31.
[264] M. Bendova, F. Gispert-Guirado, A.W. Hassel, E. Llobet, A. Mozalev, Nano Energy 33 (2017) 72–87.
[265] J. Zhang, M. Gu, X. Chen, Micro Nano Eng. 21 (2023) 100229.
[266] K. Dissanayake, D. Kularatna-Abeywardana, J. Energy Storage 96 (2024) 112563.
[267] A. Nayak, B. Bhushan, S. Kotnala, N. Kukretee, P. Chaudhary, A.R. Tripathy, K. Ghai, S. Laxmi Mudliar, Mater. Today Proc. 73 (2023) 227–232.
[268] J. Li, J. Zhu, Z. Dong, Q. Wu, Chem. Select 8 (24) (2023) e202204487.

[269] S.H. Park, Y.H. Kim, T.G. Lee, H.K. Shon, H.M. Park, J.Y. Song, Mater. Res. Bull. 47 (11) (2012) 3612–3618.
[270] A. Mozalev, M. Bendova, F. Gispert-Guirado, E. Llobet, H. Habazaki, Surf. Coat. Technol. 489 (2024) 131042.
[271] A. Mozalev, M. Bendova, R. Vazquez, Z. Pytlicek, E. Llobet, J. Hubalek, Sensors Actuators B 229 (2016) 587–598.
[272] C. Toyos-Rodríguez, D. Valero-Calvo, A. Iglesias-Mayor, A. de la Escosura-Muniz, Front. Bioeng. Biotechnol. 12 (2024).
[273] T. Sjöström, M.J. Dalby, A. Hart, R. Tare, R.O. Oreffo, B. Su, Acta Biomater. 5 (5) (2009) 1433–1441.
[274] A. El Merhie, M. Salerno, C. Toccafondi, S. Dante, Colloids Surf. B 178 (2019) 32–37.
[275] C. Drieschner, M. Minghetti, S. Wu, P. Renaud, K. Schirmer, ACS Appl. Mater. Interfaces 9 (2017) 9496–9505.
[276] T.G. Schreiner, B.I. Tamba, C.T. Mihai, A. Lőrinczi, M. Baibarac, R.C. Ciobanu, B.O. Popescu, J. Clin. Med. 11 (19) (2022) 5846.
[277] Z. Fohlerova, K. Kamnev, M. Sepúlveda, Z. Pytlicek, J. Prasek, A. Mozalev, Adv. Mater. Interfaces 8 (14) (2021) 2100256.
[278] C. Toccafondi, R. La Rocca, A. Scarpellini, M. Salerno, G. Das, S. Dante, Appl. Surf. Sci. 351 (2015) 738–745.
[279] V.Z. Zulfa, N. Nasori, U. Farahdina, M. Firdhaus, I. Aziz, H. Suprihatin, M.N. Rhomadhoni, A. Rubiyanto, Molecules 28 (2) (2023) 617.
[280] S.A. Shamsuddin, S.C. Gopinath, M. Derman, I. Jasni, C. Ibau, M.F.M. Tahir, Biochem. Eng. J. 202 (2024) 109149.